High-throughput characterization of photocrosslinker-bearing ion channel variants to map residues critical for function and pharmacology

Nina Braun[1], Søren Friis[2], Christian Ihling[3], Andrea Sinz[3], Jacob Andersen[1,#], Stephan A. Pless[1*]

[1]Department of Drug Design and Pharmacology, University of Copenhagen, Copenhagen, Denmark

[2]Nanion Technologies GmbH, Munich, Germany

[3]Department of Pharmaceutical Chemistry & Bioanalytics, Institute of Pharmacy, Charles Tanford Protein Center, Martin Luther University Halle-Wittenberg, Halle (Saale), Germany

[#]Current address: Lundbeck Research, H. Lundbeck A/S, Valby, Denmark

Short title: High-throughput analysis of ion channels containing non-canonical amino acids

* Corresponding Author:

Stephan A. Pless: stephan.pless@sund.ku.dk

Abstract

Incorporation of non-canonical amino acids (ncAAs) can endow proteins with novel functionalities, such as crosslinking or fluorescence. In ion channels, the function of these variants can be studied with great precision using standard electrophysiology, but this approach is typically labor intensive and low throughput. Here, we establish a high-throughput protocol to conduct functional and pharmacological investigations of ncAA-containing hASIC1a (human acid-sensing ion channel 1a) variants in transiently transfected mammalian cells. We introduce three different photocrosslinking ncAAs into 103 positions and assess the function of the resulting 309 variants with automated patch-clamp (APC). We demonstrate that the approach is efficient and versatile, as it is amenable to assessing even complex pharmacological modulation by peptides. The data show that the acidic pocket is a major determinant for current decay and live-cell crosslinking provides insight into the hASIC1a-psalmotoxin-1 interaction. Further, we provide evidence that the protocol can be applied to other ion channels, such as P2X2 and GluA2 receptors. We therefore anticipate the approach to enable future APC-based studies of ncAA-containing ion channels in mammalian cells.

42 **Introduction**

43 Genetic code expansion approaches allow the incorporation of non-canonical amino acids (ncAAs)
44 with unique chemical properties into proteins. Over the past two decades, this method has greatly
45 facilitated protein modification and functionalization beyond the confines of the genetic code [1]. Ion
46 channels have proven highly suited to ncAA incorporation, as evidenced by the success in
47 introducing photocrosslinking, photoswitchable or fluorescent ncAAs into numerous members of this
48 large and diverse protein family [2-4]. Among the ncAA subclasses, photocrosslinkers have proven
49 particularly versatile, as they allow for the trapping of ion channels in certain conformational states
50 [5-8], capturing of protein-protein interactions [9-12] and covalent linking of receptor-ligand
51 complexes to delineate ligand binding sites [13-17].

52

53 Typically, incorporation of ncAAs is achieved by repurposing a stop codon to encode for a ncAA
54 supplied by an orthogonal tRNA/aminoacyl tRNA synthetase (aaRS) pair. But the incorporation
55 efficiency can be variable and unspecific incorporation of naturally occurring amino acids can result
56 in inhomogeneous protein populations [2]. Verification of site-specific ncAA incorporation can
57 therefore be laborious and time-consuming, especially in combination with detailed functional
58 characterization. As a result, most studies have focused on only a limited number of incorporation
59 sites, and the evaluation of potential functional or pharmacological effects of ncAA incorporation
60 often remained minimal. In principle, automated patch-clamp (APC) devices offer fast and efficient
61 high-throughput testing and have recently gained increasing popularity for electrophysiological
62 interrogation of a diverse set of ion channels [18-22]. However, a combination of low efficiency of
63 transient transfection in mammalian cells and limited ncAA incorporation rates have thus far
64 prevented functional screening of ncAA-containing ion channel variants on APC platforms.

65

66 Here, we sought to overcome these limitations by developing a fluorescence-activated cell sorting
67 (FACS)-based approach to enrich the population of transiently transfected cells expressing ncAA-
68 containing ion channels. Using the human acid-sensing ion channel 1a (hASIC1a) as an example,
69 we incorporated three different ncAA photocrosslinkers (AzF (4-Azido-L-phenylalanine), Bpa (4-
70 Benzoyl-L-phenylalanine) and Se-AbK ((R)-2-Amino-3-{2-[2-(3-methyl-3H-diazirin-3-yl)-

71 ethoxycarbonylamino]-ethylselanyl}-propionic acid)) at 103 positions throughout its intracellular,
72 extracellular and transmembrane domains.
73 ASICs are trimeric ligand-gated ion channels that open a weakly sodium-selective pore in response
74 to proton binding to the so-called acidic pocket and likely other sites in the extracellular domain [23].
75 Apart from contributions to synaptic plasticity [24, 25], ASICs have recently gained increasing
76 attention as potential drug targets for pain and stroke [26-35]. The six different human ASIC isoforms
77 (ASIC1a, 1b, 2a, 2b, 3 and 4) are modulated by an impressive array of neuropeptides and venom-
78 derived toxins that bind to the large extracellular domain [24, 36, 37]. Intriguingly, the extent and type
79 of modulation (e.g. inhibition vs potentiation) are often highly dependent on ambient proton
80 concentration, as well as subtype and species origin [38, 39]. This poses challenges for
81 pharmacological profiling and motivates a detailed understanding of the mechanism and site of
82 action of these peptides, to eventually generate lead compounds that could potentially target pain or
83 stroke.
84
85 In this study, we establish a protocol to functionally screen ncAA-containing ion channels in
86 transiently transfected cells on an APC platform. The 384-well setup of the SyncroPatch 384PE
87 (Nanion Technologies) allows the efficient characterization of 309 hASIC1a variants and we show
88 that ncAA incorporation is tolerated in over 50% of the positions. Incorporation of bulky ncAA
89 photocrosslinkers generally results in lower pH sensitivity, especially around the acidic pocket, where
90 ncAA incorporation also greatly accelerates current decay kinetics. We further demonstrate
91 differential channel modulation by the neuropeptide big dynorphin (BigDyn; [40]) and by psalmotoxin-
92 1 (PcTx1; [41]), a toxin derived from tarantula venom. Lastly, we turn to UV-induced
93 photocrosslinking to covalently trap channel-toxin complexes and thus map the hASIC1a-PcTx1
94 interaction in live cells. Overall, our work highlights that ncAA-containing ion channels, including
95 ASICs, ionotropic glutamate and P2X receptors, are amenable to APC-based high-throughput
96 screening. We further demonstrate how this approach, when used with ncAA photocrosslinkers, can
97 be harnessed to investigate protein-peptide or protein-protein interactions *in cellulo*.

98 **Results**

99 **Development of an APC screen to validate ncAA incorporation into hASIC1a**

100 In order to efficiently assess functional incorporation of ncAAs into human ASIC1a (hASIC1a), we
101 developed an APC screen to record proton-gated channel activation (Figure 1). To this end, we co-
102 transfected 103 different hASIC1a variants containing individual TAG stop codons throughout the
103 protein together with the suppressor tRNA/ncAA-RS pair for either AzF, Bpa or Se-AbK and a GFP-
104 reporter carrying a TAG at Y40 (for Bpa and Se-AbK) or Y151 (for AzF, as we observed a higher
105 degree of unspecific incorporation in the Y40TAG variant with AzF) into custom-made ASIC1a-KO
106 HEK 293T cells [17, 42-44]. The corresponding ncAA was supplied in the cell culture medium six
107 hours after transfection or omitted from the experiment in incorporation control samples. To increase
108 cell viability and uptake efficiency, we synthesized the methylester derivates of AzF and Bpa [8, 45].
109 This allowed us to supplement the cell media with 50- and 100-fold lower ncAA concentration
110 compared to previous studies, respectively [7, 13].
111 After 48 hours, cells grown in the presence of ncAA were sorted for green fluorescence to enrich the
112 population of transfected cells, which were then submitted to APC to record proton-gated currents.
113 Using GFP fluorescence as a proxy, we determined a transfection efficiency of 62.9 ± 9.5% for
114 hASIC1a WT and an average of 11.2 ± 5% for the ncAA variants (Figure S1, Table S1). Without the
115 FACS step, the latter rate would translate into less than 10% of the APC wells being occupied by
116 transfected cells, precluding efficient APC experiments. By contrast, the cell sorting improves
117 occupation to around 46% of wells with successful patch also displaying proton-gated currents (62%
118 for AzF, 29% for Bpa and 48% for Se-AbK) and is therefore an indispensable element for the use of
119 transiently transfected cells in APC (Figure S1).
120 The 384-well system of the SyncroPatch 384PE allows for parallel concentration response curve
121 measurements on 24 different samples, enabling us to test 11 different channel variants with
122 corresponding incorporation controls (cells grown in the absence of ncAA), as well as hASIC1a WT
123 and untransfected cells in less than one hour, with up to 16 replicates per sample. Specifically, we
124 embarked to functionally interrogate 103 positions throughout the hASIC1a sequence: 38 positions
125 in the N-terminal domain (Figure S2), 24 positions in the transmembrane domain and interface

126 region (Figure S3), 29 positions in the C-terminal domain (Figure S4) and 12 positions around the
127 acidic pocket (Figure 3 and S8). The current traces in Figure 2A show typical pH-induced inward
128 currents of hASIC1a WT with a pH_{50} of 6.64 ± 0.12 (n=182), in line with previous studies [46, 47], as
129 well as a variant with lower proton sensitivity containing AzF in the acidic pocket (T236AzF, pH_{50}
130 6.17 ± 0.14, n=10). Interestingly, the incorporation of Bpa, AzF and Se-AbK at position W46 did not
131 result in proton-gated currents (Figure 2A, Figure S3), despite a previous report showing functional
132 incorporation of a bulky ncAA at this conserved Trp in the M1 helix [48]. We analysed all variants for
133 mean peak current size and pH_{50} to compare incorporation efficiency and proton sensitivity,
134 respectively (Figures S2-4 and S8, Table S1). Furthermore, we routinely assessed the extent of
135 tachyphylaxis [49] and variants displaying >20% current decrease after reaching the peak current
136 are indicated in Figures 3 and S2-8 as well as Table S1.
137 To provide a comprehensive overview, we mapped incorporation patterns for the three
138 photocrosslinkers onto snake plots schematically depicting an ASIC1a subunit (Figure 2B-D). We
139 defined specific incorporation (circles with dark colour shade) as proton-gated currents of >1 nA
140 observed in the presence of ncAA, and minimal (<500 pA) proton-gated currents in the absence of
141 ncAA. If currents >500 pA were observed in the absence of ncAA, incorporation was considered
142 unspecific (circles with lighter colour shade), while positions labelled in grey did not yield substantial
143 currents in either condition (<1 nA). However, we cannot exclude the possibility of underestimating
144 the degree of unspecific incorporation, as enriching transfected cells grown in the absence of ncAA
145 by FACS was not feasible due to the low number of cells displaying GFP fluorescence (2.2 ± 1.7%).
146 On the other hand, by defining incorporation as not successful for currents <1 nA, we are aware that
147 we may have potentially excluded variants in which specific ncAA incorporation resulted in reduced
148 open probability or lower conductance.
149 As is apparent from the snake plots, we observed robust incorporation in the N-terminus, around the
150 acidic pocket and in the proximal C-terminus. Indeed, among the 80 positions tested up to and
151 including L465, AzF resulted in functional channel variants in 61% of cases, compared to 50% for
152 Bpa and 44% for Se-AbK (Figure 2E).
153

154

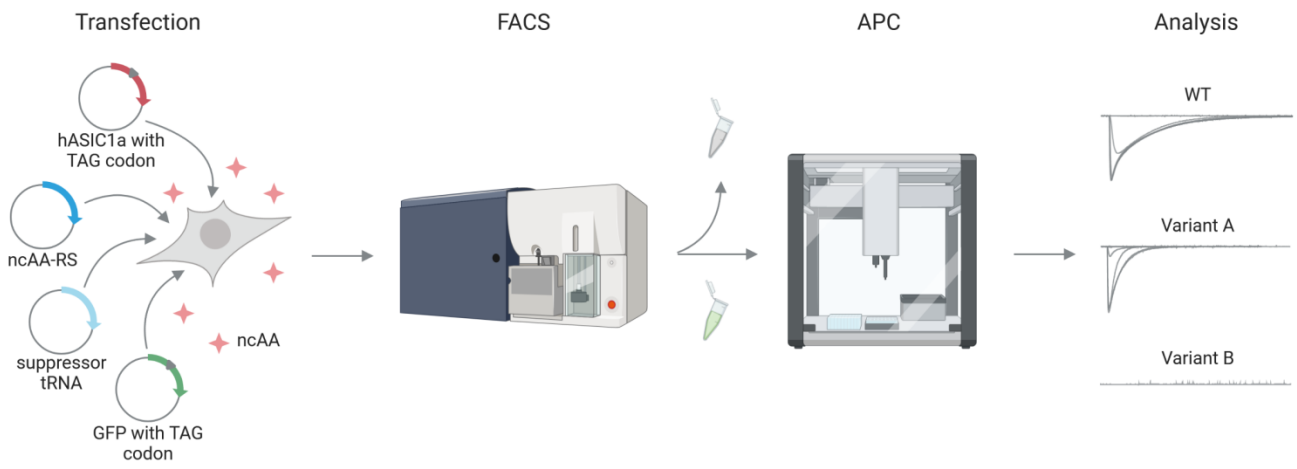

155

156 *Figure 1: Schematic illustration of the workflow to assess ncAA incorporation into hASIC1a.*
157 *HEK 293T ASIC1a-KO cells are transfected with hASIC1a containing a TAG stop codon at the site*
158 *of interest, a co-evolved suppressor tRNA/ncAA-RS pair and a TAG-containing GFP reporter. ncAA*
159 *is supplied in the cell culture medium. 48 hours after transfection, cells are sorted for green*
160 *fluorescence on a FACS BD Aria I and those showing fluorescence are subjected to APC on a*
161 *SyncroPatch 384PE to measure proton concentration response curves.*
162

163 By contrast, all three crosslinkers showed mostly unspecific incorporation distal of L465, with WT-
164 like current phenotypes from position 467 onwards (Figure S4 and S5A-C). This led us to
165 hypothesize that channel constructs truncated in this region are functional. To investigate this further,
166 we inserted an additional TGA stop codon for several variants, confirmed channel truncation by
167 comparing molecular weight on a Western blot and measured concentration response curves in APC
168 and two electrode voltage-clamp (TEVC) (Figure S5D-E). We found that channels truncated after
169 H463 or K464 yielded no current in either APC or TEVC, but truncation after L465 produced a variant
170 with strong tachyphylaxis in HEK 293T cells (Figure S5D) and truncation after C466 or R467 resulted
171 in channels with WT-like proton sensitivity in both APC and TEVC. We conclude that the C-terminus
172 distal of position 465 is not essential for proton-gated channel activity and that it is not possible to
173 differentiate between currents originating from truncated and full-length protein to evaluate ncAA
174 incorporation. We therefore added a C-terminal 1D4-tag to the hASIC1a construct to selectively
175 purify full-length protein and compare the amounts in cells grown in the presence or absence of
176 ncAA. This strategy confirms efficient incorporation in the distal C-terminus (Figure S6A).

177 Additionally, liquid chromatography/tandem mass spectrometry data revealed that Bpa can be
178 specifically incorporated at positions distal of L465 (A480, Figure S6B).
179 For the 80 positions up to and including L465, we evaluated incorporation efficiency by comparing
180 how many positions could be functionally replaced by each of the ncAA photocrosslinkers, based on
181 the nature of the side chain occupying the position in the native channel and the position within the
182 protein overall. We did not find evidence for pronounced global trends, but for instance Bpa
183 incorporation was tolerated best at originally aromatic side chains (79%), while replacement of basic
184 residues was least successful (27%) (Figure 2E). The three tested prolines could not be exchanged
185 for any of the ncAAs. Interestingly, and in contrast to our expectations, Se-AbK incorporation only
186 produced functional variants in 33% of cases when replacing structurally similar Lys and Arg side
187 chains, while success rates were higher at polar and acidic side chains (58% and 54%, respectively).
188 AzF incorporation rates were similar throughout all protein domains, whereas Bpa was better
189 tolerated in the transmembrane regions and less in the N- and C-termini and Se-AbK incorporation
190 in the M2 helix and C-terminus was negligible (Figure 2E). Overall, incorporating the three
191 photocrosslinkers produced functional variants in all protein domains, albeit with varying success
192 rates.
193 Together, we show that combining FACS with APC affords the time-efficient functional
194 characterization of over 300 hASIC1a variants and provides a versatile platform to assess successful
195 ncAA incorporation throughout all protein domains.
196 To evaluate if the established APC screen can also serve as a platform for other ion channels, we
197 applied it to selected TAG variants of the rat P2X2 and rat GluA2 receptors. Specifically, we
198 compared currents upon exposure to two different concentrations of ATP or glutamate, respectively
199 (Figure S7 and Table S2, [5, 7, 50]). Incorporation of AzF into position K296 of the rP2X2 receptor
200 is unspecific, whereas that of Bpa is efficient and specific (Figure S7A). For GluA2, incorporation
201 patterns at Y533 and S729 are identical to those observed in previous studies using manual patch-
202 clamp (Figure S7B, [5, 7]). Incorporation of AzF at Y533 is tolerated with currents of 1.21 ± 0.96 nA
203 (n=30, compared to 600 ± 100 pA (n=15) reported by Poulsen *et al.*), while incorporation of Bpa does
204 not produce a functional channel. At position S729, we observe small currents of 390 ± 330 pA for
205 AzF (n=17) and 280 ± 240 pA for Bpa (n=16, compared to 470 ± 50 pA reported by Klippenstein *et*

206 *al.* for S729Bpa). Importantly, as GluA2 gating is fast compared to the perfusion speed of the
207 SyncroPatch 384PE and Klippenstein *et al.* report increased desensitization rates for S729 variants,
208 we pre-incubated cells with 100 µM cyclothiazide to slow desensitization and increase the likelihood
209 of resolving the GluA2 peak current [51]. While our GluA2 and P2X2 data show that target-specific
210 optimization of the ligand-application protocols is required, they illustrate that our APC screening
211 approach can be applied to a variety of different ion channels and yields results comparable to those
212 obtained with conventional ncAA-incorporation protocols.

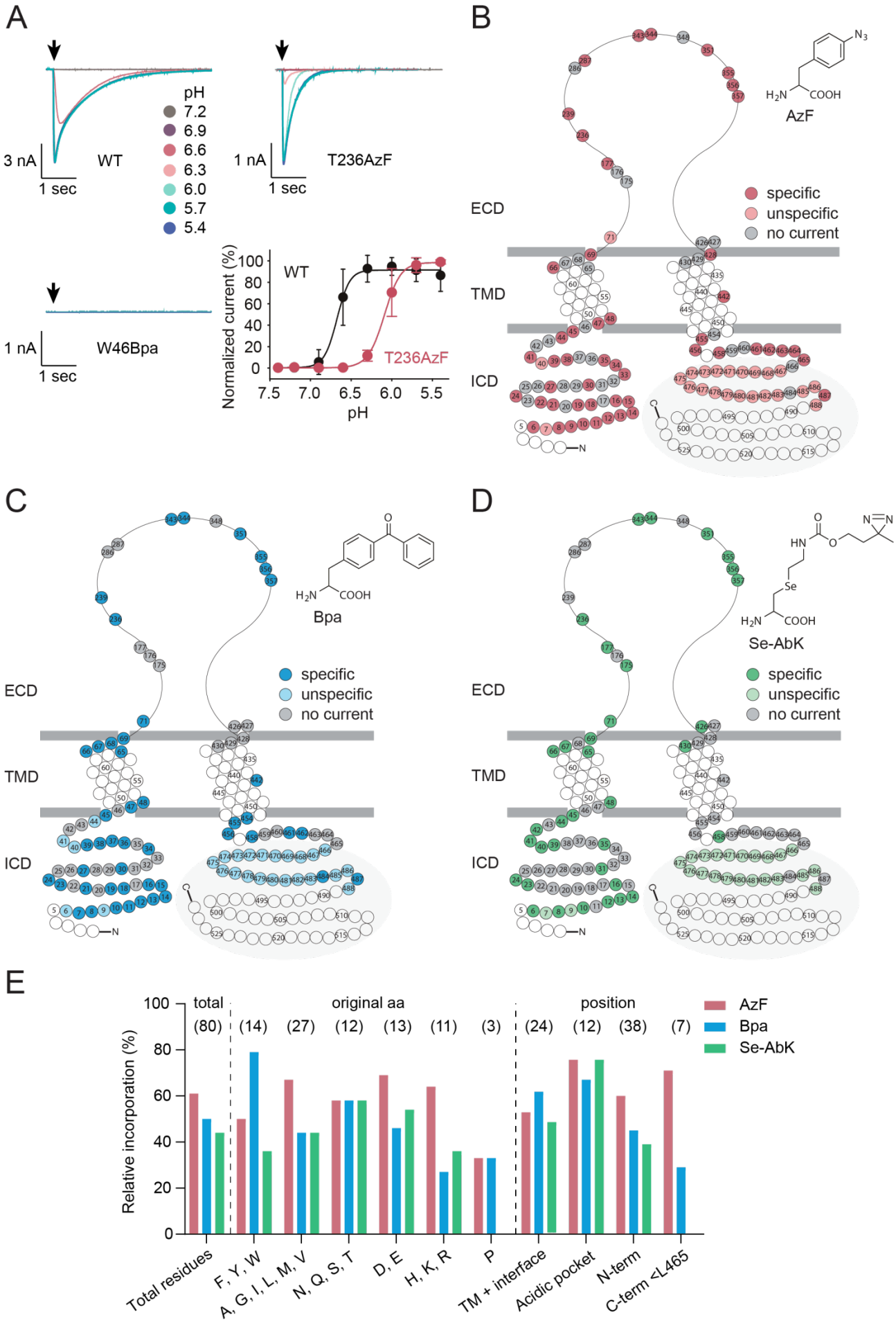
A
pH
7.2
6.9
6.6
6.3
6.0
5.7
5.4
3 nA
1 sec
WT
1 nA
1 sec
T236AzF
1 nA
1 sec
W46Bpa
Normalized current (%)
WT
T236AzF
pH
B
AzF
ECD
TMD
ICD
specific
unspecific
no current
C
Bpa
ECD
TMD
ICD
specific
unspecific
no current
D
Se-AbK
ECD
TMD
ICD
specific
unspecific
no current
E
Relative incorporation (%)
total
original aa
position
AzF
Bpa
Se-AbK
Total residues
F, Y, W
A, G, I, L, M, V
N, Q, S, T
D, E
H, K, R
P
TM + interface
Acidic pocket
N-term
C-term <L465

213

214 *Figure 2: Incorporation of ncAA crosslinkers is tolerated in all domains of hASIC1a and produces*
215 *functional channel variants. (A) Representative current traces for pH response curves of hASIC1a*
216 *WT, T236AzF and W46Bpa recorded on the SyncroPatch 384PE, pH response curve in bottom right*
217 *corner (WT pH_{50} 6.64 ± 0.12, n=182; T236AzF pH_{50} 6.17 ± 0.14, n=10). (B-D) Snake plot*
218 *representations indicating specific, unspecific and unsuccessful incorporation (no current) for AzF*
219 *(B), Bpa (C) and Se-AbK (D). Specific incorporation (circles with darker shade) is defined as pH-*
220 *dependent peak currents >1 nA observed in cells grown in the presence, but not in the absence of*
221 *ncAA, whereas unspecific incorporation (circles with lighter shade) indicates that currents were*
222 *observed both in the presence and absence of ncAA. Positions indicated by grey circles did not yield*
223 *functional channel variants when replaced by an ncAA (no current), while those coloured in white*
224 *were not tested. The grey area highlights positions distal of L465. (E) Relative incorporation rates of*
225 *AzF (red), Bpa (blue) and Se-AbK (green) at 80 different hASIC1a positions. Exchanged amino acids*
226 *are grouped for original side chain properties and position within the channel, respectively (TM:*
227 *transmembrane helices; N-term: N-terminus; C-term <L465: C-terminus up to and including L465).*
228 *Relative incorporation rates were calculated by dividing the number of positions successfully*
229 *replaced with a ncAA by the total number of positions at which incorporation was attempted.*
230 *Positions distal of L465 were excluded from the analysis (highlighted in grey in B-D), as more distal*
231 *deletions result in truncated, but functional channels (see Figures S4-6).*

232 **Photocrosslinker incorporation in the acidic pocket decreases proton sensitivity and**
233 **accelerates current decay**

234 During the design of the construct library for the APC screen, we consulted the 2.8 Å resolution
235 structure of PcTx1 bound to chicken ASIC1 (PDB 4FZ0) to select 12 positions around the acidic
236 pocket that are in sufficiently close proximity to potentially form covalent crosslinks with PcTx1 if
237 replaced by a ncAA [52] (Figure S8A). Most of the resulting ncAA channel variants were functional,
238 but in several instances, the initially applied proton concentration range of up to pH 5.4 did not yield
239 saturating currents (Figure S8B/C). Consequently, we re-evaluated these variants using a lower pH
240 range to resolve the pH_{50} and re-assess peak current size (Figure 3). This allowed us to determine
241 EC_{50} values for all variants and confirmed that hASIC1a variants containing ncAAs in the acidic
242 pocket display markedly reduced proton sensitivity, with pH_{50} values as low as 5.49 ± 0.13
243 (T239Bpa, mean ± S.D., n=6) and 5.66 ± 0.26 (D357AzF, mean ± S.D., n=10). Additionally, we
244 observed substantial changes in current shape compared to WT. For example, current decay rates
245 were increased for T239Bpa (t½ 224 ± 176 ms, n=6) and D357AzF (t½ 93.8 ± 40.9 ms, n=10)

compared to WT (t½ 818 ± 750 ms, n=9), indicating possible effects of the photocrosslinkers on channel gating (rates of desensitization or closure, Figure 3B and Table S3). Overall, we found that incorporation of Se-AbK was least efficient, so all subsequent experiments focused on AzF- and Bpa-containing channel variants.

As hASIC1a variants with ncAAs around the acidic pocket displayed markedly altered proton sensitivity and current decay rates, we next wanted to assess if these variants can still be modulated by two peptide gating modifiers that interact with the acidic pocket, BigDyn and PcTx1.

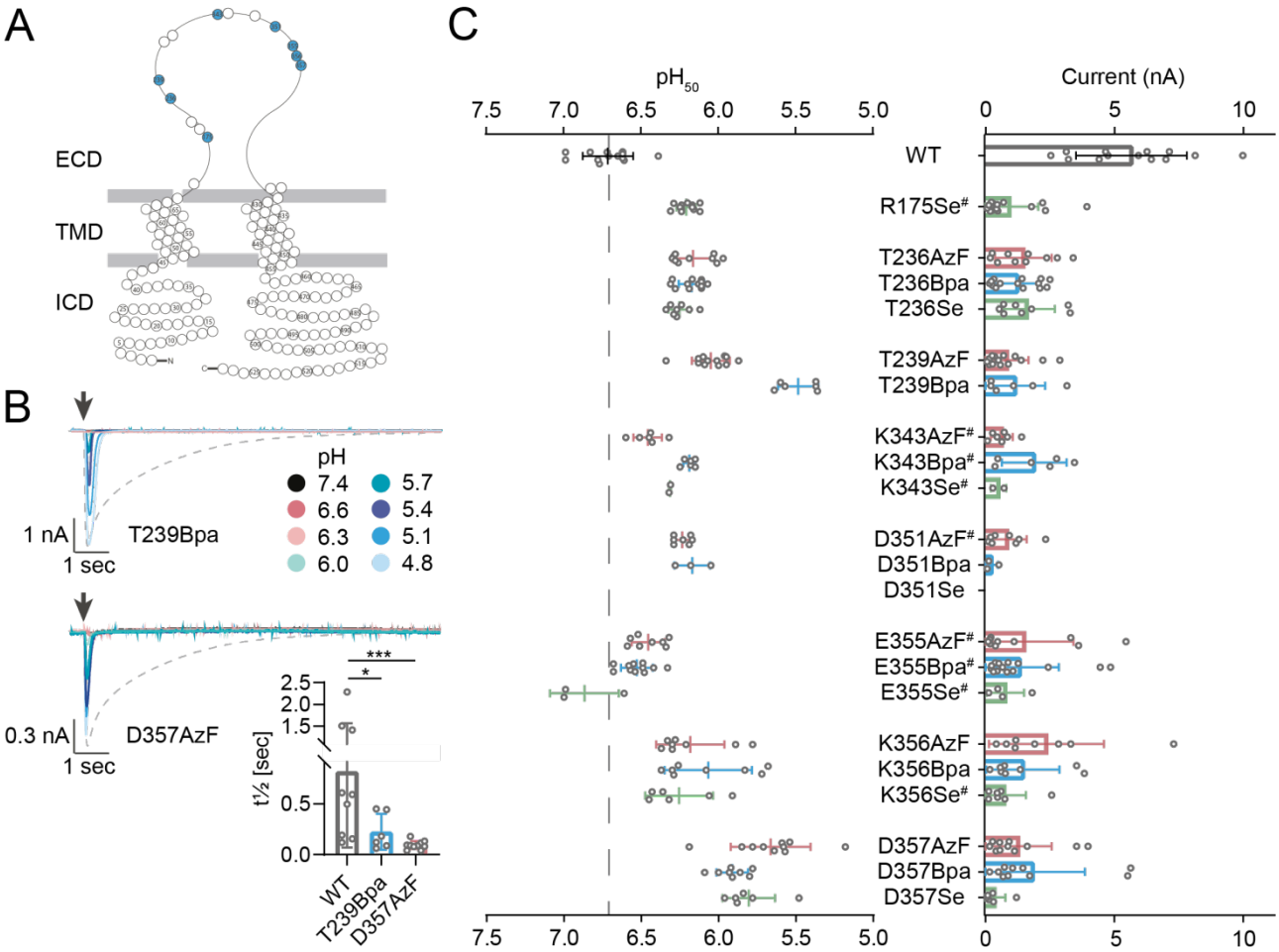

Figure 3: Incorporation of ncAA photocrosslinkers into the acidic pocket results in channel variants with lowered proton sensitivity and accelerated current decay. (A) Snake plot of hASIC1a with the assessed positions highlighted in blue. (B) Representative current traces of variants T239Bpa and D357AzF as recorded on the SyncroPatch 384PE, with arrows indicating the time of proton application. Dashed lines indicate WT current in response to pH 6.0 application. Bar graph shows mean t½ ± S.D. of current decay. (C) Incorporation of AzF (red), Bpa (blue) and Se-AbK (green) at 8 positions around the acidic pocket results in lowered proton sensitivity for several variants. Dot plots comparing pH_{50} (left) and peak current sizes (right), bars indicate mean ± S.D., (#) indicates

262 *>20% tachyphylaxis (see also Figure S8 and Table S1), (*) denotes significant difference between*
263 *t½ of current decay, p < 0.05; (***): p < 0.001; Mann-Whitney test (see also Table S3).*

264 **Peptide modulation is retained in hASIC1a variants containing photocrosslinkers in the**
265 **acidic pocket**

266 First, we investigated the neuropeptide BigDyn, which interacts with the acidic pocket and shifts the
267 proton dependence of both activation and SSD [17]. A key physiological function of BigDyn is to limit
268 ASIC1a steady-state desensitization (SSD) [40]. In order to define the appropriate pH for BigDyn
269 application on each variant, we first established an APC-based protocol to determine SSD curves.
270 Due to the open-well system of the SyncroPatch 384PE, lowering the conditioning pH to assess SSD
271 required multiple mixing steps, which we simulated on a pH meter to determine the apparent pH the
272 cells are exposed to before each activation (Figure S9). Using this approach, we obtained a pH_{50}
273 SSD of 6.91 ± 0.02 for hASIC1a WT (n=40), which is lower than the value reported in *Xenopus laevis*
274 oocytes (pH_{50} SSD = 7.05 ± 0.01, Figure S10A+B). Notably, we also observed a more shallow Hill
275 slope for WT compared to oocytes (n_H 3.16 ± 0.42 vs 9.45 ± 2.84), but not for any of the tested
276 variants in the acidic pocket or interface region (Figure S10B-F, Table S4). SSD profiles of the ncAA-
277 containing variants varied with pH_{50} SSD values ranging from 7.15 ± 0.01 (E177Bpa, n=12) to 6.76
278 ± 0.06 (K356AzF, n=7, Table S4), with most variants displaying a slightly increased proton sensitivity
279 compared to WT. This is in contrast to the observed pattern of reduced proton sensitivity for proton-
280 gated activation, suggesting that incorporation of ncAA photocrosslinkers in the acidic pocket
281 modulates proton sensitivity of activation and SSD differentially. For our subsequent APC
282 experiments to assess BigDyn modulation, we chose a conditioning pH that led to around 10%
283 remaining current upon activation.
284 Here, we focused on AzF-containing variants for which we had previously detected crosslinking to
285 BigDyn on Western blots to evaluate if the observed peptide-channel interaction also results in
286 functional modulation [17]. Cells were exposed to SSD-inducing pH conditions in the presence or
287 absence of 3 µM BigDyn and the resulting currents upon pH 5.6 activation were normalized to control
288 currents after incubation at pH 7.6 (Figure 4A+B). Control cells not exposed to BigDyn exhibited SSD
289 to 0-30% mean remaining current (Figure S11, Table S5), while BigDyn co-application during

290 conditioning limited SSD to varying degrees (Figure 4B). BigDyn increased rescue from pH-induced
291 SSD in all tested AzF-containing variants, but did not do so in WT, despite a similar trend (Figure 4B).
292 For all tested variants, we regularly observed incomplete SSD after the first conditioning step, but
293 this typically increased after the second conditioning step (see Figure S11). This could point towards
294 possible confounding effects by the repeated solution mixing to achieve the desired conditioning pH
295 described above. However, despite the reduced control over the conditioning pH compared to using
296 a perfusion system with continuous flow, it was still possible to determine if BigDyn modulates
297 hASIC1a SSD. In short, the APC setup enables rapid evaluation of several channel variants with
298 different SSD profiles for BigDyn modulation in a single experiment.
299

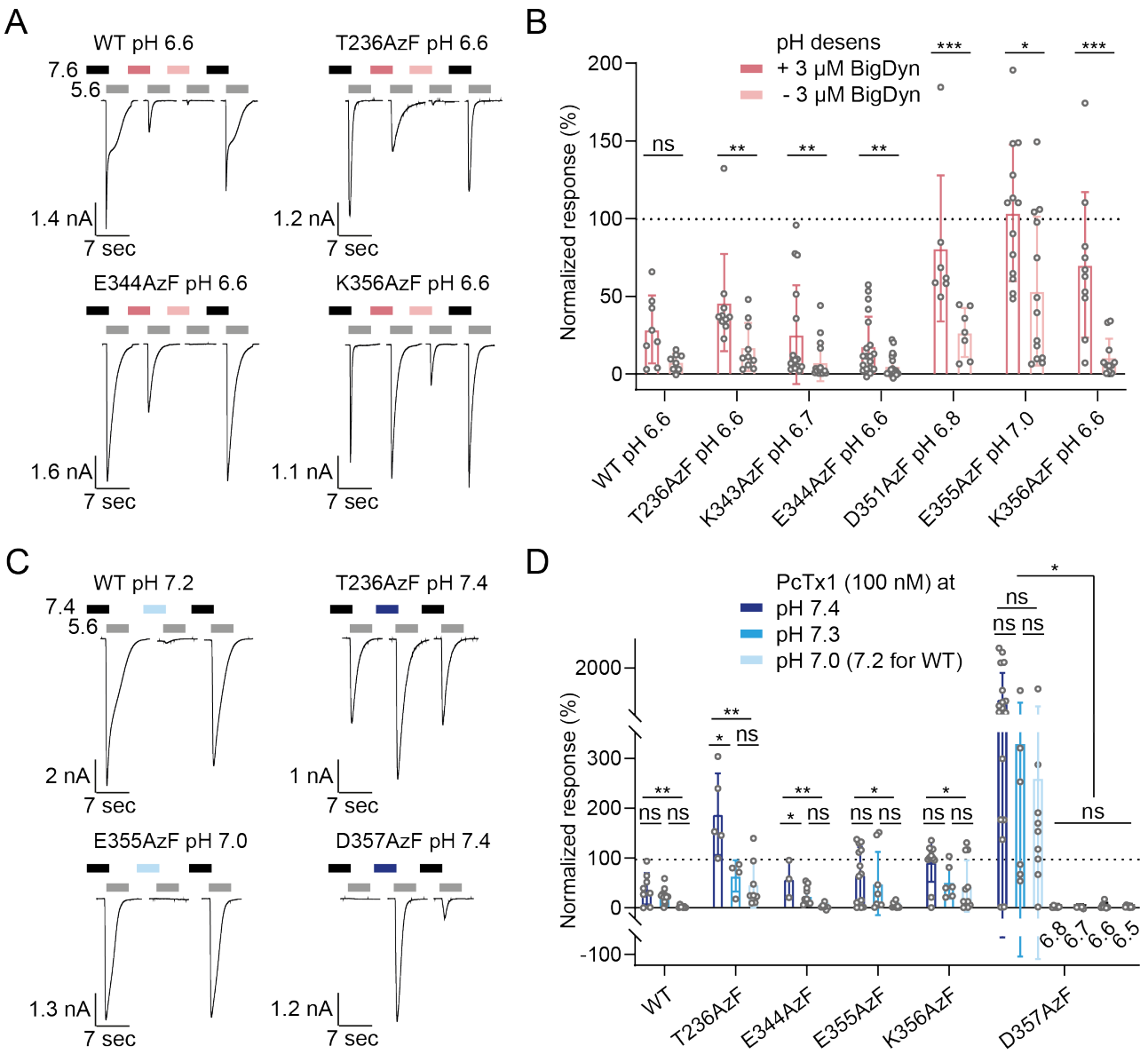

300

301 *Figure 4: Peptide modulation of hASIC1a WT and selected variants containing AzF in the acidic*
302 *pocket. (A) Characteristic current traces and (B) normalized response after SSD in absence or*
303 *presence of BigDyn for hASIC1a WT and six ncAA variants. Cells were incubated at the*
304 *desensitizing pH specified for each variant with or without 3 µM BigDyn for 2 min (pink bars) before*
305 *activation at pH 5.6 (grey bars, 5 sec) and the currents were normalized to the average of two control*
306 *currents after conditioning at pH 7.6 (black bars; control traces shown in Figure S11). (C) Exemplary*
307 *current traces and (D) bar graph for PcTx1 modulation of hASIC1a WT and selected variants*
308 *containing AzF in the acidic pocket at different pH. Cells were incubated with 100 nM PcTx1 at*
309 *varying pH for 2 min (blue bars) before activation at pH 5.6 (grey bars, 5 sec) and the current was*
310 *normalized to the average of the four preceding and following control currents after conditioning at*
311 *pH 7.4 (black bars). Bar graphs show mean ± S.D, dashed line indicates 100%, values in Table S5*
312 *and S6. (*) denotes significant difference between groups, $p < 0.05$; (**): $p < 0.01$; (***): $p < 0.001$;*
313 *ns: not significant; Mann Whitney test (B) or one-way ANOVA with Tukey's multiple comparisons*
314 *test (D). Coloured and black bars in (A) and (C) not to scale.*
315
316 We next tested a subset of AzF-containing acidic pocket variants for modulation by the gating
317 modifier PcTx1, which was originally isolated from the venom of the *Psalmopoeus cambridgei*
318 tarantula [41]. PcTx1 has previously been shown to increase the apparent proton affinity of both
319 activation and steady-state desensitization of ASIC1a, resulting in inhibition or potentiation,
320 depending on the application pH [39, 41, 53, 54]. Here, we assessed hASIC1a modulation by co-
321 applying 100 nM PcTx1 at varying conditioning pH and compared the resulting current upon
322 activation with pH 5.6 to the average of the preceding and following control currents after
323 conditioning at pH 7.4 (Figure 4C). For hASIC1a WT, we observed increasing inhibition from
324 38.2 ± 31.7% of current remaining at pH 7.4 to 2.06 ± 2.50% at pH 7.2 (Figure 4D, Table S6). This
325 is in agreement with previous findings that the PcTx1 IC_{50} decreases at lower pH values [39].
326 Channel variants with AzF in positions 344, 355 or 356 showed a similar trend (Figure 4D). In
327 contrast, we saw potentiation for T236AzF at pH 7.4 and for D357AzF at pH 7.4 to 7.0 (Figure 4C+D).
328 This is consistent with the observation that these variants are among those with most pronounced
329 reduction in the pH_{50} of activation (Figure 3, S8 and Table S1, pH_{50} 6.17 ± 0.14 (n=10) and
330 5.66 ± 0.26 (n=10), respectively). D357AzF in particular exhibited an unusual phenotype: the first
331 two control applications of pH 5.6 led to only very small or no detectable channel activation, but pH
332 5.6 after pre-application of the toxin induced a substantial inward current, after which the channels
333 also activated in response to the following control applications. We therefore chose to evaluate

334 PcTx1 modulation of D357AzF in more detail. Specifically, we used lower pH during conditioning
335 and observed that at pH 6.8 and below, the variant is inhibited. In light of the strong potentiation at
336 pH 7.0, this highlights that PcTx1 modulation of D357AzF exhibits a striking pH dependence, which
337 far exceeds that of WT and the other mutants examined here (Figure 4D, Table S6) [39].
338 Overall, the APC assay established here enabled the time-efficient characterization of
339 pharmacological modulation of selected hASIC1a variants, providing an overview on their PcTx1
340 modulation profile at different application pH. Together, these results confirm that hASIC1a variants
341 containing ncAA photocrosslinkers in the acidic pocket can still be modulated by known peptide
342 gating modifiers, opening avenues to efficiently study peptide-channel interactions with a
343 combination of APC and photocrosslinking.

344 **Photocrosslinking confirms PcTx1 binding to the hASIC1a acidic pocket**

345 Nine out of the originally targeted 12 positions around the PcTx1 binding site exhibited specific AzF
346 incorporation (Figure 5A, left inset) and were used for photocrosslinking experiments followed by
347 Western blotting following the workflow in Figure 5B. In parallel, six positions in the lower
348 extracellular domain, F69, Y71, V80, D253, W287 and E413 were also replaced by AzF to confirm
349 the specificity of potential photocrosslinking around the acidic pocket. (Figure 5A, right insets).
350 hASIC1a variants were expressed in HEK293T ASIC-KO cells and 100 nM biotinylated PcTx1 was
351 added before cells were exposed to UV light (365 nm) for 15 min to induce photocrosslinking. We
352 then isolated full-length hASIC1a via a C-terminal 1D4-tag and analysed protein samples on a
353 Western blot with antibodies against biotin and the 1D4-tag to detect PcTx1 and hASIC1a,
354 respectively. Biotinylated PcTx1 was absent in UV-exposed hASIC1a WT and in all control positions
355 containing AzF in the lower extracellular domain (F69, Y71, V80, D253, W287 and E413), as well as
356 in samples containing AzF in the acidic pocket not exposed to UV light (Figure 5C). By contrast,
357 PcTx1 was detected at four out of nine AzF-containing positions (344, 355, 356 and 357) after UV
358 exposure, indicating covalent photocrosslinking at these positions (marked in red in Figure 5A), but
359 at none of the five other sites in the acidic pocket tested (marked in green).
360

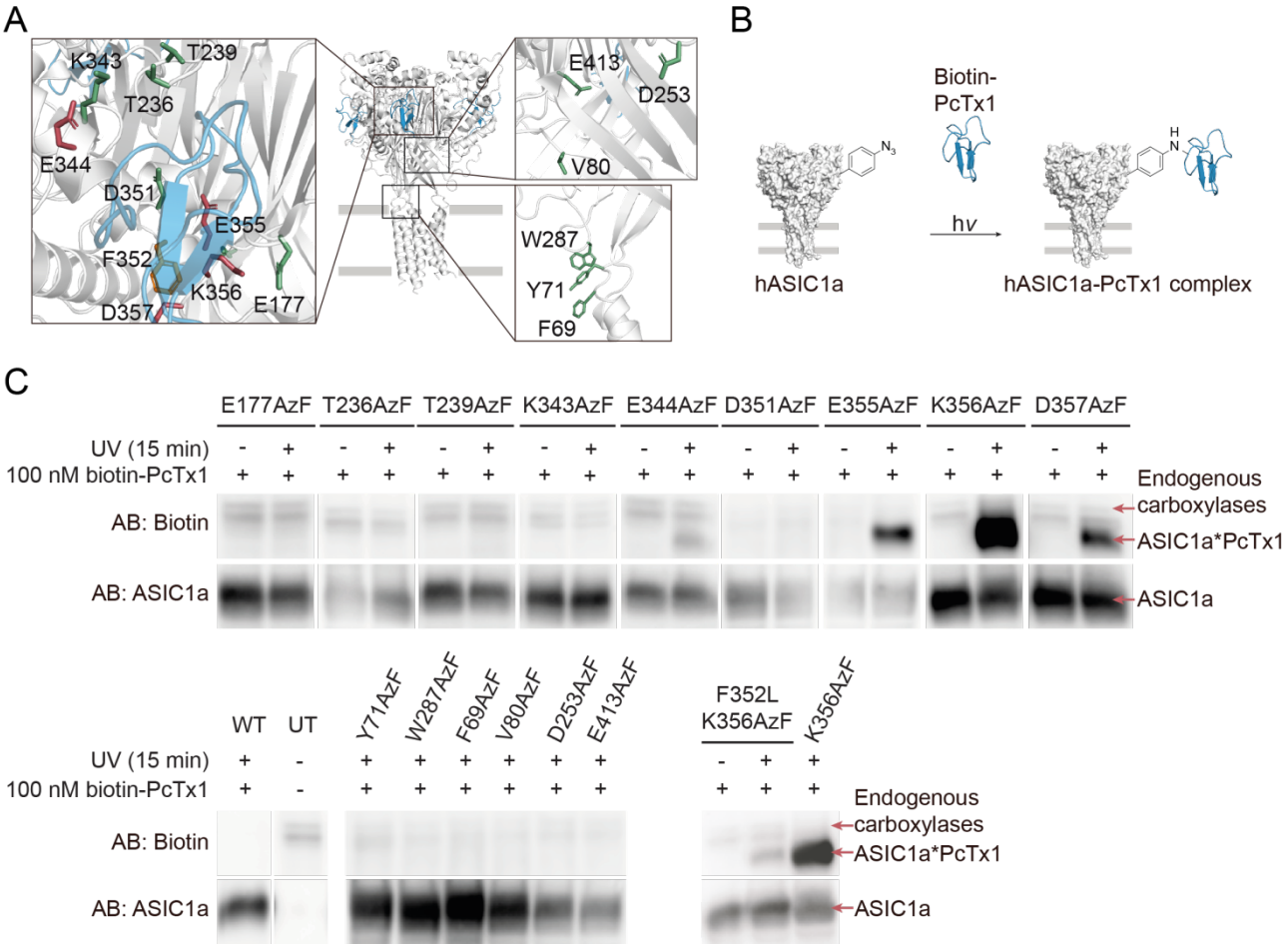

Figure 5: Live-cell photocrosslinking delineates the PcTx1 binding site at the ASIC1a acidic pocket. (A) Structure of cASIC1 (white) in complex with PcTx1 (blue, PDB: 4FZ0), insets show individual side chains replaced by AzF in the acidic pocket (left inset) and lower extracellular domain (right insets). Positions that crosslinked to biotin-PcTx1 are coloured red, F352 is marked in orange and positions that did not crosslink are coloured green. (B) Schematic workflow for crosslinking to biotin-PcTx1. HEK 293T ASIC1a-KO cells expressing AzF-containing hASIC1a variants are incubated with 100 nM biotin-PcTx1 and exposed to UV light for 15 min to form covalent hASIC1a-PcTx1 complexes, which are purified via a C-terminal 1D4-tag on hASIC1a and visualized via Western blotting. (C) Western blot of purified hASIC1a WT, untransfected cells (UT) and variants carrying AzF in the extracellular domain detected using the specified antibodies (AB). Biotin-PcTx1 is detected in UV-exposed samples containing AzF at positions 344, 355, 356 and 357 in the acidic pocket (coloured red in A, left inset), but not at positions 177, 236, 239, 343 or 351 (coloured green in A, left inset). PcTx1 is also absent in control samples not exposed to UV, those carrying AzF in the lower extracellular domain (right insets in A), WT or UTs. PcTx1 can be detected upon UV-exposing the toxin-insensitive F352L K356AzF double mutant (left inset in A, F352 coloured orange). Of note, the anti-biotin AB detects endogenous biotin-dependent carboxylases, which are also found in purified samples from UTs and have been described before [55, 56]. Data is representative of

379 *three individual experiments, see Figures S12-15 for original blots and crosslinking attempts with*
380 *Bpa.*
381
382 Previous studies have shown that the F352L mutation at the base of the acidic pocket eliminates the
383 modulatory effect of PcTx1 on hASIC1a [57, 58], but it remained unclear if the toxin is still able to
384 bind to hASIC1a. To test this possibility directly, we combined the F352L mutation with one of the
385 crosslinking variants, resulting in the hASIC1a F352L K356AzF double mutant variant. Upon UV
386 exposure, we were able to detect the PcTx1-hASIC1a complex even in the presence of the F352L
387 mutation, albeit in lower amounts as assessed by the lower band intensity compared to the K356AzF
388 single variant (Figure 5C, lower panel). This suggests that the F352L mutation does not eliminate
389 toxin binding *per se*, but likely primarily abolishes the functional effects caused by PcTx1.
390 Attempts to photocrosslink PcTx1 using Bpa in the equivalent positions around the acidic pocket did
391 not succeed (Figure S12). We therefore tested PcTx1 modulation of selected Bpa variants on the
392 SyncroPatch 384PE to assess if the toxin binds to the acidic pocket when Bpa is present (Figure
393 S13, Table S6). We observed robust inhibition at pH 7.0, indicating the interaction persists despite
394 incorporating a bulky ncAA within the acidic pocket. However, most of the variants showed only weak
395 modulation at the pH used during the UV exposure (7.4), which might partly explain the lack of
396 crosslinking with Bpa.
397 Overall, our photocrosslinking experiments confirm that PcTx1 interacts with the acidic pocket of
398 hASIC1a, even in the presence of a mutation that abolishes the functional effects of PcTx1.
399

400 **Discussion**

401 *First comprehensive functional assessment of ncAA-containing ion channels on an APC platform*

402 Since their introduction, APC platforms have greatly aided ion channel research with their high
403 throughput capabilities [59]. However, the requirement for high transfection rates to express the ion
404 channels of interest limits the types of experiments that can be performed with this approach. Our
405 FACS-assisted ncAA incorporation assay represents, to our knowledge, the first example of using
406 an APC platform to functionally interrogate ncAA-containing ion channels. By transiently transfecting
407 the protein of interest into mammalian cells and selecting those that express all components with
408 FACS, we circumvent the need for stable cell lines. This method therefore greatly expands the scope
409 of experiments that can be addressed using APC-based approaches.

410 Our extensive scanning of 309 ncAA-containing variants emphasizes the amenability of hASIC1a to
411 ncAA incorporation, with the highest tolerance observed for AzF (61% functional variants) followed
412 by Bpa (50%) and Se-AbK (44%) (Figure 2E). Previous studies on incorporation of AzF and Bpa into
413 the human serotonin transporter (hSERT) and α-amino-3-hydroxy-5-methyl-4-isoxazolepropionic
414 acid receptor (AMPAR) also show preferred functional incorporation of AzF and attribute this to its
415 smaller size [7, 13]. Rannversson *et al*. report lowest ncAA tolerance in the hSERT TMD (44% and
416 20% for AzF and Bpa, respectively), contrasting our findings in the TM segments of hASIC1a (52%
417 and 61%). However, it should be noted that we specifically selected the outer turns of the TM helices,
418 where the study on AMPARs observed better incorporation compared to the more tightly packed
419 central pore [7].

420 Previous work on hSERT shows higher success rates for replacing aromatic vs non-aromatic side
421 chains, a trend we only observe for Bpa. Generally, genetic encoding of ncAAs does not appear to
422 depend on the original properties of the replaced amino acid when assessed via protein expression
423 [14, 60]. Indeed, a systematic examination of the effect of the similarly bulky ncAA acridonylalanine
424 on protein solubility found no correlation to amino acid conservation, hydrophobicity or accessibility,
425 but a close dependence on the location within the overall tertiary structure [61]. Consequently, the
426 authors suggest that scientists broaden rather than narrow screens when aiming to introduce a ncAA
427 into a new target protein. In the present study, we cover around 20% of hASIC1a and functionally

428 assess three different ncAAs, likely the most comprehensive investigation of genetic code expansion
429 in a transmembrane protein to date.
430
431 *Mechanistic insights into ASIC function*
432 A beneficial side-effect of replacing native side chains with ncAA photocrosslinkers is that, in addition
433 to their photoactivatable properties, these bulky side chains can also inform on basic biophysical
434 aspects of the protein domain in question. Here, we show that incorporation of bulky, non-polar side
435 chains leads to functional channels in about 50% of all cases, and we observe a general trend
436 towards lower apparent proton affinity in the ncAA-bearing hASIC1a channels. This is particularly
437 evident at positions in or near the acidic pocket, where previous studies have shown that mutations
438 to acidic side chains in thumb and finger domains result in increased pH_{50} values (reviewed in [23]).
439 By contrast, we only found a few positions in M1 (L45, Q66, F69) that resulted in higher apparent
440 proton affinity. This is consistent with previous work on the nearby pre-M1 region [62], as well as a
441 number of M1 and M2 mutations that mostly resulted in left-shifted pH_{50} values [48, 63]. Together,
442 this suggests that mutations in M1 and M2 of ASIC1a have a general tendency to increase apparent
443 proton affinity.
444 Generally, we observe that the time course of current decay is relatively heterogeneous (Figure 2
445 and 3, S7), likely due to the slow and incomplete solution exchange (see also below). This makes
446 an exact quantification of the changes to activation or desensitization rates difficult. Nevertheless,
447 we observe that the same sites around the acidic pocket that show a pronounced decrease in
448 apparent proton affinity also display a marked acceleration in current decay rates ($t_{1/2}$ analysis in
449 Figure 3B, S8 and Table S3). This was consistently observed at all of the eight sites around the
450 acidic pocket assessed in Figure 3 and was independent of the nature of the incorporated ncAA.
451 This finding is coherent with a previous study that showed the thumb domain affects rates of fast
452 desensitization [64]. Alternatively, it is conceivable that the observed phenotype is due to greatly
453 increased channel deactivation rates [65]. Although we cannot discriminate between these
454 possibilities, our data clearly show that the physico-chemical properties of side chains lining the
455 acidic pocket are a major determinant for current decay in ASIC1a.

456 We also noticed varying degrees of tachyphylaxis, especially when positions in the external turns of
457 the TM helices were replaced with ncAAs (Figure S3, Table S1). In light of previous work suggesting
458 a contribution by permeating protons and an effect of hydrophobicity of TM1 side chains on
459 tachyphylaxis, this warrants further investigation [49, 66].
460
461 *Complex pharmacological modulation studied in ncAA-containing channels using APC*
462 The complex pharmacological modulation pattern of hASIC1a by BigDyn and PcTx1 is notoriously
463 challenging to study. However, we were able to optimize the APC protocols to replicate and even
464 expand on the differential effects of this highly state-dependent peptide modulation (Figure 4).
465 Specifically, we were able to show that despite the prominently lowered proton sensitivity of acidic
466 pocket variants, all tested ncAA-containing hASIC1a variants retained some degree of modulation
467 by both BigDyn and PcTx1. We observed varying degrees of BigDyn-dependent rescue from SSD
468 for the different variants (Figure 4B). Under our conditions, rescue from SSD was incomplete when
469 we applied 3 µM BigDyn, a concentration well above the reported EC_{50} range of 26-210 nM [17, 40].
470 In combination with the steep pH dependence of modulation, this resulted in considerable variability
471 in the BigDyn modulation data, as evident by the reported range in S.D. values. While this can, at
472 least in part, be attributed to our limited control over the BigDyn-application pH, we have made similar
473 observations in a previous study using TEVC [17].
474 PcTx1 inhibited or potentiated AzF-containing hASIC1a variants in a pH dependent manner, in line
475 with previous reports [39]. We examined a total of five variants, of which all except T236AzF also
476 formed covalent complexes with the toxin upon UV exposure (Figure 5C). While PcTx1 still
477 modulates and therefore interacts with hASIC1a T236AzF (Figure 4C+D), we cannot exclude that
478 introduction of AzF at positions 177, 239, 343 or 351 prevents toxin interaction, as these variants
479 were not assessed for PcTx1 modulation with APC and did not crosslink to the peptide upon UV
480 exposure (Figure 5C).
481
482 *Live-cell crosslinking provides a detailed map of the PcTx1-hASIC1a interaction*
483 The acidic pocket is now well established both as a hotspot for channel activation and as a binding
484 site for pharmacological modulators [17, 23]. In the case of PcTx1, structural data had already

485 outlined the toxin binding site on ASICs [52, 67], but unlike previous work, the crosslinking approach
486 outlined in this study enables us to covalently trap ligand-channel complexes in living cells. This
487 represents a notable advantage, especially for highly state-dependent interactions, such as those
488 between hASIC1a and BigDyn or PcTx1. Additionally, comparing the crosslinking pattern between
489 two ligands, the approach can indirectly inform on the varying degrees of conformational flexibility of
490 the ligands: BigDyn is likely to be highly flexible without a strong propensity to adopt a secondary
491 fold [68, 69], therefore samples a greater conformational space and is thus more likely to undergo
492 covalent crosslinking at multiple sites (9/9 sites tested at the acidic pocket, [17]). By contrast, PcTx1
493 folds into a compact and highly stable conformation and will consequently undergo covalent
494 crosslinking at relatively fewer sites (4/9 sites tested at the acidic pocket, Figure 5). These findings
495 also complement an earlier investigation of the key interactions between PcTx1 and ASIC1a that
496 concluded for the majority of contacts observed in the crystal structures to not persist during MD
497 simulations or to not be functionally relevant for PcTx1-mediated inhibition of ASIC1a [58].
498 The ability to covalently trap ligand-receptor complexes offers a unique opportunity to directly assess
499 if ASIC mutations shown to alter or abolish ligand effects still bind to the same site on the receptor.
500 For example, the hASIC1a F352L mutation at the base of the acidic pocket is known to almost
501 completely abolish the PcTx1-dependent modulation of ASIC1a channels [57, 58]. Yet it remained
502 unclear if the toxin also interacts with the acidic pocket in these mutant channels. Here, we directly
503 demonstrate that PcTx1 still binds to the acidic pocket, even at a concentration that is far too low to
504 have a functional effect on the mutant channels (100 nM). This leads us to propose that the F352L
505 mutation primarily affects conformational changes responsible for the PcTx1 effect on WT hASIC1a,
506 but not toxin binding *per se*.
507 We note that unlike AzF, we were unable to employ Bpa for crosslinking experiments with PcTx1.
508 To test if introduction of the more bulky photocrosslinker prevents toxin interaction, we assessed
509 PcTx1 modulation of selected variants with APC and found robust inhibition for most variants,
510 indicating that Bpa does not fully occlude the acidic pocket (Figure S13). We therefore speculate
511 that steric constraints due to the positioning of the benzophenone diradical and the more selective
512 reactivity of Bpa (reacts exclusively with C-H bonds) may play a role [70, 71]. Together, this

513 emphasizes that screens with multiple redundant ncAAs significantly increase chances of observing
514 successful crosslinking.
515
516 *Limitations of the outlined APC-based approach*
517 While our work establishes that ncAA-containing ion channels can be screened on an APC platform,
518 some limitations persist. Firstly, our present approach relies on simultaneous transfection of four
519 plasmids (Figure 1), which can negatively impact transfection efficiency and/or result in cells not
520 containing all four components. Careful optimization of DNA amounts and transfection conditions is
521 therefore necessary and a revised construct design to reduce the number of plasmids could further
522 improve yields. For example, the Plested group achieved co-expression of TAG-containing AMPAR
523 and GFP with an internal ribosome entry site (IRES) [5, 7], while Rook *et al.* used ASIC1a with a C-
524 terminally fused GFP-tag [8]. Furthermore, both Zhu and co-workers and Rook *et al.* created
525 bidirectional plasmids to encode both AzF-RS or Bpa-RS and tRNA, respectively [6, 8]. This latter
526 strategy might be particularly fruitful for the incorporation of Se-AbK, which was generally less
527 efficient than that of AzF and Bpa (Figure 2E and Table S1), despite others reporting robust
528 incorporation of a similar ncAA [72].
529 Secondly, while GFP fluorescence indicates successful transfection and ncAA incorporation and
530 thereby increased likelihood of observing proton-gated currents in cells grown in the presence of
531 ncAA, it is not a reliable proxy for incorporation specificity in control cells grown in the absence of
532 ncAA. This is due to the fact that the degree of unspecific incorporation in GFP does not correlate
533 with that of the ncAA-containing hASIC1a variants. We consistently observed GFP fluorescence in
534 only around 2% of the control cells, independent of the co-expressed channel variant, which
535 translated to insufficient cell numbers for APC (requires a minimal concentration of 100.000 cells/ml).
536 Assuming that the transfection rates are similar in the presence and absence of ncAA (i.e. around
537 11%, Figure S1B), we concluded that recording a larger number of unsorted control cells is the more
538 stringent approach to assess incorporation efficiency. We therefore did not subject the incorporation
539 control cells to FACS and instead conducted APC with the entire unsorted cell population. To
540 evaluate this strategy, we randomly selected 45 hASIC1a variants assessed for ncAA incorporation
541 in the N-terminus, ECD or C-terminus and compared the number of wells harbouring a patched cell

542 with >100 MΩ seal and those showing proton-gated currents in presence and absence of ncAA
543 (Figure S1C). While the percentage of cells with current is generally lower for cells grown in the
544 absence of ncAA, we do observe currents for those positions where incorporation is unspecific, e.g.
545 throughout the C-terminus and in some positions in the N-terminus. For the control samples, an
546 average of 9.8 out of 16 possible wells contained a cell with >100 MΩ seal, and we observed currents
547 in 1.6 wells on average. We therefore conclude that despite some shortcomings, the employed
548 strategy using non-sorted controls detects at least those positions with unspecific incorporation of
549 >15% (i.e. 1.6/9.8).
550 Thirdly, while APC platforms offer unprecedented throughput and speed, there are limitations with
551 regards to the rate and extent of perfusion exchange. This can be particularly challenging for ligand
552 application to fast-gating ligand-gated ion channels (i.e. pH changes for ASIC1a) in general and
553 strongly state-dependent pharmacological modulation (by e.g. BigDyn or PcTx1) in particular.
554 Although we were able to partially overcome these issues by employing a solution stacking
555 approach, we cannot draw detailed conclusions about activation or desensitization kinetics.
556 Similarly, values for proton-dependent activation and especially SSD can be determined with greater
557 precision using TEVC or manual patch-clamp electrophysiology. However, note that the values
558 reported here are generally in agreement with previous reports, both with regards to WT values [46,
559 47] and relative shifts caused by mutations, i.e. in the acidic pocket [23].
560 Lastly, limitations arise from the accessibility and running costs of APC platforms compared to
561 conventional patch-clamp set ups. But we anticipate that the establishment of academic core
562 facilities for high-throughput electrophysiology (e.g. Northwestern University, Il, US; University of
563 Nantes, France; Illawarra Health and Medical Research Institute, Wollongong, Australia) and
564 collaborations between academia and industry (this study, [73-76]) will likely contribute to a broader
565 accessibility. This is also evident from the rising number of publications involving APC (currently >80
566 publications according to vendor information).
567
568 *Conclusions and outlook*
569 The ability to functionally screen ncAA-containing ion channels on APC platforms has the potential
570 to greatly expand the use of ncAAs in both academic and industry settings. The intrinsically high

571 throughput enables rapid assessment of incorporation efficiencies, functional properties and even
572 complex pharmacological modulation. In principle, the approach can be used for both site-specific
573 (this study) and global ncAA incorporation [77, 78], thus further increasing the number and type of
574 chemical modifications that can be introduced. In the case of incorporation of photocrosslinking
575 ncAAs, the approach can be exploited to crosslink to peptides (Figure 5, [17]), small molecules [13]
576 or establish intra-protein crosslinking, including in protein complexes [8, 9]. Furthermore, the recently
577 developed ability for on-chip optostimulation on related APC platforms [79] offers exciting prospects
578 for potentially conducting UV-mediated crosslinking during live APC experiments in the future. Paired
579 with MS and/or biochemical approaches [80, 81], the overall strategy could also be expanded to
580 define interaction sites of unknown or known protein-protein interactions. Given that there are now
581 well over 100 different ncAAs available for incorporation into proteins in mammalian cells [1, 82], the
582 above approach will enable the efficient study of ion channels endowed with a wide range of
583 properties or functionalities.

584 **Material and Methods**

585 **Molecular biology.** The complementary DNA (cDNA) encoding human ASIC1a (hASIC1a) was
586 kindly provided by Dr. Stephan Kellenberger. Plasmids containing AzF-RS, Bpa-RS and tRNA were
587 gifts from Dr. Thomas P. Sakmar [43]. AbK-RS and $tRNA_{pyl}$ in pcDNA3.1 were kindly provided by Dr.
588 Chris Ahern [44]. The dominant negative eukaryotic release factor (DN-eRF) was a gift from Dr.
589 William Zagotta [83]. Plasmids containing rat GluA2 Q607 Y533TAG or S729TAG were gifts from
590 Dr. Andrew Plested [5, 7], rat GluA2 Q607 WT was kindly provided by Dr. Anders Skov Kristensen.
591 Rat P2X2 WT 3T was a gift from Dr. Thomas Grutter [50], the K296TAG variant was generated in-
592 house.
593 Site-directed mutagenesis was performed using PfuUltraII Fusion polymerase (Agilent, Denmark)
594 and custom DNA mutagenesis primers (Eurofins Genomics, Germany). All sequences were
595 confirmed by sequencing of the full coding frame (Eurofins Genomics). For hASIC1a constructs, a
596 C-terminal 1D4-tag was added for protein purification and Western blot detection and two silent
597 mutations were inserted at V10 and L30 to reduce the risk of potential reinitiation [84].
598
599 **Cell culture and transfection.** HEK 293T cells (ATCC®), in which endogenous hASIC1a was
600 removed by CRISPR/Cas9 [17], were grown in monolayer in T75 or T175 flasks (Orange Scientific,
601 Belgium) in DMEM (Gibco, Denmark) supplemented with 10 % FBS (Thermo Fisher Scientific,
602 Denmark) and 1 % penicillin-streptomycin (Thermo Fisher Scientific) and incubated at 37 ˚C in a
603 humidified 5 % CO_2 atmosphere. For APC experiments, cells were seeded into six-well plates
604 (Orange Scientific) at a density of 300.000 cells/well and transfected the next day with Trans-IT LT1
605 (Mirus, WI, USA) and 1:1:1:1 µg DNA encoding hASIC1a TAG variants, ncAA-RS, tRNA and eGFP
606 Y40TAG or Y151TAG, respectively. For the WT control, cells were transfected with 1 µg hASIC1a
607 WT and 0.3 µg eGFP WT. Six hours after transfection, cell medium was replaced with supplemented
608 DMEM containing 10 µM AzF- or Bpa-methylester (synthesis in SI) or 100 µM Se-AbK (custom-
609 synthesized by ChiroBlock, Germany). FACS and APC recordings were performed 48 hours after
610 transfection. The same procedure was used for GluA2 and P2X2R recordings.
611 For crosslinking studies, cells were seeded into 15 cm dishes (VWR, Denmark) at a density of 5-7
612 million cells and transfected the next day with PEI (Polysciences, Germany) and 16:4:4:8 µg DNA

613 encoding hASIC1a TAG variants, AzF-RS, tRNA and DN-eRF, respectively. For WT controls,
614 2 million cells were seeded into a 10 cm dish (VWR) and transfected with 8 µg hASIC1a WT. Six
615 hours after transfection, cell medium was replaced with supplemented DMEM containing 0.5 mM
616 AzF (Chem Impex, IL, USA) or 1 mM Bpa (Bachem Bio, Switzerland) and crosslinking studies were
617 performed 48 hours after transfection. Please note that for crosslinking studies followed by Western
618 blot, the free acid version of the ncAAs was used to increase protein yields.
619
620 **FACS**. HEK 293T cells were washed with PBS, treated with Accutase (Sigma Aldrich, Denmark) or
621 Trypsin-EDTA (Thermo Fisher Scientific), pooled and centrifuged at 1000 rpm for 5 min. They were
622 resuspended in 350 µl of a 1:1 mixture of serum-free Hams F-12 nutrient mixture and extracellular
623 patch-clamp solution (140 mM NaCl, 4 mM KCl, 1 mM $MgCl_2$, 2 mM $CaCl_2$, 10 mM HEPES, pH 7.4)
624 supplemented with 20 mM HEPES and transported to the FACS core facility at ambient temperature.
625 A FACSAria I or III (BD Biosciences, CA, USA) with a 70 µm nozzle was used to sort cells for
626 singularity, size and GFP fluorescence (Excitation 488 nm, Emission 502 nm (low pass) and 530/30
627 nm (band pass)). Cells were filtered through a sterile 50 µm cup filcon (BD Biosciences) directly
628 before sorting to prevent clogging of the nozzle. The WT control was used to set the fluorescence
629 cutoff between GFP-positive and GFP-negative populations and to check the purity of the sort before
630 sorting 1 million GFP-positive cells for subsequent patch-clamp experiments. Where possible, a
631 minimum of 200000 GFP-positive cells were collected for hASIC1a TAG variants grown in presence
632 of ncAA, while controls grown in absence of ncAA and untransfected cells were not sorted. Cells
633 were collected in 1.5 ml tubes containing the 1:1 mixture mentioned above and transported to the
634 APC instrument at ambient temperature.
635
636 **Automated patch-clamp.** Automated whole-cell patch-clamp recordings were conducted on a
637 SyncroPatch 384PE (Nanion Technologies, Germany) directly after FACS sorting. Cells were loaded
638 into a teflon-coated plastic boat at concentrations of 1 million cells/ml (WT, controls grown in absence
639 of ncAA and untransfected cells) or 200000–400000 cells/ml (variants grown in presence of ncAA)
640 and incubated at 20 °C and 200 rpm. For patch-clamp recordings, a NPC®-384 medium resistance
641 single hole chip (Nanion Technologies) was filled with intracellular solution (120 mM KF, 20 mM KCl,

642 10 mM HEPES, pH 7.2) and extracellular solution (140 mM NaCl, 4 mM KCl, 1 mM $MgCl_2$, 2 mM
643 $CaCl_2$, 10 mM HEPES, pH 7.4). 30 µl of cells were loaded into each well and the cells were caught
644 on the holes by brief application of -200 mbar pressure and washed with 30 µl seal enhancer solution
645 (extracellular solution with 8 mM Ca^{2+}) under a holding pressure of -50 mbar. After a wash step with
646 extracellular solution, two more pulses of -200 mbar were applied to reach whole cell configuration
647 and the cells were clamped at 0 mV under atmospheric pressure (Figure S9A). For recordings of
648 concentration-response curves, extracellular solutions at different pH were applied using a liquid
649 stacking approach. Briefly, pipette tips were loaded with 45 µl of pH 7.4 wash solution followed by
650 5 µl of activating extracellular solution (pH 7.2-4.8). For each sweep, the baseline current was
651 recorded for 1 sec before application of the 5 µl activating solution, while the pH 7.4 wash solution
652 was dispensed with a delay of 5 sec to allow for recording of channel opening and desensitization in
653 the presence of ligand. The second dispension was directly followed by aspiration of liquid and a
654 second wash step with pH 7.4 before application of the next activating pH (interval between stimuli
655 140 sec, Figure S9B).
656 For SSD curve recordings, cells were exposed to an activating pH of 5.6 using the stacked addition
657 protocol described above, while the conditioning pH was varied (pH 7.6-6.4). The open-well system
658 of the SyncroPatch 384PE does not allow a single exchange of the entire liquid surrounding the cell,
659 as this would result in destabilization or loss of the seal. Instead, the conditioning pH was adjusted
660 stepwise by repeated addition and removal of 50% of the solution in the well, leading to 6 min
661 conditioning intervals between stimuli (Figure S9C). While this process was simulated at the pH
662 meter to determine the apparent conditioning pH, small variations may occur due to mixing effects.
663 The authors note that APC instruments operating with microfluidic flow channels might offer superior
664 control of the conditioning pH. At the end of each SSD curve recording, a control application of pH
665 5.6 after conditioning pH 7.6 was used to assess the extent of current rescue and exclude cells that
666 did not recover from SSD.
667 For peptide modulation experiments, 0.1 % (w/v) bovine serum albumin (BSA, Sigma Aldrich) was
668 added to the conditioning solutions to reduce peptide loss on boat and tip surfaces. To investigate
669 modulation by BigDyn (synthesis described in [17]), cells were first exposed to two activations with
670 pH 5.6 after conditioning at pH 7.6 to determine the control current, followed by two rounds of

671 activation after 2 min conditioning with a pH that induces SSD (total interval between stimuli: 8 min,
672 due to the conditioning protocol described above) and a control activation to evaluate current
673 recovery. For half of the cell population, 3 μM BigDyn were co-applied during the second conditioning
674 period to measure rescue from SSD. This assessment of SSD and recovery was repeated with
675 peptide co-application during the first SSD-conditioning to also evaluate peptide wash out. To assess
676 modulation by PcTx1 (Alomone labs, Israel, >95% purity), cells were exposed to two control
677 measurements of activation with pH 5.6 after conditioning at pH 7.4 (interval 3.75 min), followed by
678 pH 5.6 activation after incubation with 100 nM PcTx1 at varying pH (pH 7.4-7.0) for 2 min (total
679 interval between stimuli 7 min), as well as two further controls to assess recovery from modulation.
680 For recordings on GluA2 and P2X2R variants, cells were clamped at -60 mV and currents activated
681 by application of 30 μM and 300 μM/10 mM ATP or glutamate, respectively. Cells expressing GluA2
682 were pre-incubated with 100 μM cyclothiazide (in 0.8% (v/v) DMSO) for 60 sec before activation to
683 slow desensitization (total interval between stimuli: 220 sec) [51].
684
685 **Data analysis.** Current traces were acquired at 2 kHz and filtered in the DataControl384 software
686 using a Butterworth 4th order low pass filter at 45 Hz to remove solution artefacts. Only cells with
687 initial seals >100 MΩ were considered for biophysical characterization using GraphPad Prism 7 or
688 8, while wells with lower seals, no current or no caught cell were excluded. The relatively low seal
689 cutoff in combination with the large proton-gated currents (up to 10 nA) recorded for WT and some
690 of the ncAA-containing variants resulted in suboptimal voltage-clamp conditions for a subpopulation
691 of cells, as also apparent from the current shapes. However, we have no evidence that this adversely
692 affected activation parameters or pharmacological modulation. Where possible, APC data was
693 pooled from a minimum of three cells and two separate recording days. On several occasions, an *n*
694 of five or more was acquired during the first screening trial, in which case the experiment was not
695 repeated. Current sizes were normalized to the respective control currents and half-maximal
696 concentrations (EC_{50} values) and Hill slopes (n_H) calculated using equation (1). pH_{50} values were
697 calculated in Excel using equation (2). All values are expressed as mean ± S.D. (Standard
698 Deviation). The extent of tachyphylaxis for each recording was calculated by subtraction of the
699 normalized current at lowest pH from the normalized maximal current (> 20 % tachyphylaxis is

700 marked by ($^{\#}$)). Bar graphs and dot plots were made using GraphPad Prism 7 or 8 and SigmaPlot
701 13.0, while current traces were exported to Clampfit 10.5 and Adobe Illustrator CC 2019.

702 Equation (1): $$Y = \frac{100*\left(EC_{50}{}^{Hillslope}\right)}{\left(EC_{50}{}^{Hillslope}+\left(X^{Hillslope}\right)\right)}$$

703 Equation (2): $pH_{50} = -\log_{10}(EC_{50}[M])$

704 Mean current sizes and pH_{50} values of different cell lines and constructs were compared using
705 student's t-test, Mann Whitney test or one-way ANOVA followed by Tukey's multiple comparisons
706 test.

707

708 **Crosslinking studies, protein purification, western blotting.** Cells were washed with PBS and
709 dislodged using cell scrapers (Orange Scientific). After centrifugation (1000 rpm, 5 min), cell pellets
710 were resuspended in 1 mL PBS pH 7.4 containing 100 nM biotinyl-PcTx1 (Phoenix Pharmaceuticals,
711 CA, USA) and transferred into 12 well plates (Orange Scientific). Cells were placed on ice and
712 crosslinked at a distance of 7-10 cm to a Maxima ML-3500 S UV-A light source (Spectronics
713 corporation, 365 nm) for 15 min (AzF) or up to 60 min (Bpa). Control samples without UV exposure
714 were kept at 4 °C. After crosslinking, cells were centrifuged (1000 rpm, 5 min) and resuspended in
715 1 mL solubilisation buffer (50 mM Tris-HCl, 145 mM NaCl, 5 mM EDTA, 2 mM DDM, pH 7.5)
716 supplemented with cOmplete™ EDTA-free protease inhibitor cocktail (Sigma Aldrich). Cells were
717 lysed (2 h, 4 °C) and centrifuged for 30 min (18000 g/4 °C). In parallel, 40 µL Dynabeads Protein G
718 (Thermo Fisher Scientific) were washed with 200 µL PBS/0.2 mM DDM and incubated with 4 µg
719 RHO 1D4 antibody (University of British Columbia) in 50 µL PBS/0.2 mM DDM on a ferris wheel
720 (VWR, 30 min). After washing the beads PBS/0.2 mM DDM (with 200 µL), the cell lysate supernatant
721 was incubated with the beads on a ferris wheel (4 °C, 90 min). Beads were washed with 200 µL PBS
722 three times to remove nonspecifically bound proteins and incubated in 25 µL elution buffer (2:1
723 mixture between 50 mM glycine, pH 2.8 and 62.5 mM Tris-HCl, 2.5 % SDS, 10 % Glycerol, pH 6.8)
724 supplemented with 80 mM DTT at 70 °C for 10 min. Protein samples (12 µL) were mixed with 3 µL
725 5 M DTT and 5 µL 4x NuPAGE™ LDS sample buffer (Thermo Fisher Scientific) and incubated (95
726 °C, 20 min) before SDS-PAGE using 3–8 % Tris-Acetate protein gels (Thermo Fisher Scientific).
727 After transfer onto PVDF membranes (iBlot 2 Dry Blotting System, Thermo Fisher Scientific) and

728 blocking in TBST/3% non-fat dry milk for 1 hour, hASIC1a was detected using RHO 1D4 antibody (1
729 µg/µL, University of British Columbia) and 1:5000 goat anti-mouse IgG HRP-conjugate (Thermo
730 Fisher Scientific). Biotinyl-PcTx1 was detected using 1:1000 rabbit anti-biotin antibody (abcam, UK)
731 and 1:5000 goat anti-rabbit IgG HRP-conjugate (Promega, Denmark). Samples used for
732 incorporation controls were treated as above, but were not exposed to UV light.

733 **Funding**

734 We acknowledge the Lundbeck Foundation (R139-2012-12390 to SAP and R218-2016-1490 to NB),
735 the Boehringer Ingelheim Fond (to NB) and the University of Copenhagen for financial support.
736

737 **Acknowledgements**

738 We acknowledge the FACS core facility at the Biotech Research & Innovation Center (University of
739 Copenhagen) for technical support. We thank Dr. Iacopo Galleano for the synthesis of AzF- and
740 Bpa-ME, Dr. Christian Bernsen Borg for the synthesis of big dynorphin and members of the Pless
741 laboratory for comments on the manuscript. Figure 1 was created with BioRender.com.
742

743 **Competing interests**

744 Søren Friis is a full-time employee of Nanion Technologies. The other authors declare no competing
745 interests.

746

747 **References**

748 1. Chin JW. Expanding and reprogramming the genetic code. Nature. 2017;550(7674):53-60.
749 doi: 10.1038/nature24031. PubMed PMID: 28980641.
750 2. Braun N, Sheikh ZP, Pless SA. The current chemical biology tool box to study ion channels.
751 J Physiol. 2020. doi: 10.1113/JP276695. PubMed PMID: 32715480.
752 3. Paoletti P, Ellis-Davies GCR, Mourot A. Optical control of neuronal ion channels and
753 receptors. Nat Rev Neurosci. 2019. doi: 10.1038/s41583-019-0197-2. PubMed PMID: 31289380.
754 4. Klippenstein V, Mony L, Paoletti P. Probing Ion Channel Structure and Function Using Light-
755 Sensitive Amino Acids. Trends Biochem Sci. 2018;43(6):436-51. doi: 10.1016/j.tibs.2018.02.012.
756 PubMed PMID: 29650383.
757 5. Klippenstein V, Ghisi V, Wietstruk M, Plested AJ. Photoinactivation of glutamate receptors
758 by genetically encoded unnatural amino acids. J Neurosci. 2014;34(3):980-91. doi:
759 10.1523/JNEUROSCI.3725-13.2014. PubMed PMID: 24431456.
760 6. Zhu S, Riou M, Yao CA, Carvalho S, Rodriguez PC, Bensaude O, et al. Genetically encoding
761 a light switch in an ionotropic glutamate receptor reveals subunit-specific interfaces. Proc Natl Acad
762 Sci U S A. 2014;111(16):6081-6. doi: 10.1073/pnas.1318808111. PubMed PMID: 24715733;
763 PubMed Central PMCID: PMCPMC4000820.
764 7. Poulsen MH, Poshtiban A, Klippenstein V, Ghisi V, Plested AJR. Gating modules of the
765 AMPA receptor pore domain revealed by unnatural amino acid mutagenesis. Proc Natl Acad Sci U
766 S A. 2019;116(27):13358-67. doi: 10.1073/pnas.1818845116. PubMed PMID: 31213549; PubMed
767 Central PMCID: PMCPMC6613130.
768 8. Rook ML, Williamson A, Lueck JD, Musgaard M, Maclean DM. beta11-12 linker isomerization
769 governs acid-sensing ion channel desensitization and recovery. Elife. 2020;9. doi:
770 10.7554/eLife.51111. PubMed PMID: 32031522; PubMed Central PMCID: PMCPMC7041949.
771 9. Murray CI, Westhoff M, Eldstrom J, Thompson E, Emes R, Fedida D. Unnatural amino acid
772 photo-crosslinking of the IKs channel complex demonstrates a KCNE1:KCNQ1 stoichiometry of up
773 to 4:4. Elife. 2016;5. doi: 10.7554/eLife.11815. PubMed PMID: 26802629; PubMed Central PMCID:
774 PMCPMC4807126.
775 10. Westhoff M, Murray CI, Eldstrom J, Fedida D. Photo-Cross-Linking of IKs Demonstrates
776 State-Dependent Interactions between KCNE1 and KCNQ1. Biophys J. 2017;113(2):415-25. doi:
777 10.1016/j.bpj.2017.06.005. PubMed PMID: 28746852; PubMed Central PMCID: PMCPMC5529200.
778 11. Martin GM, Rex EA, Devaraneni P, Denton JS, Boodhansingh KE, DeLeon DD, et al.
779 Pharmacological Correction of Trafficking Defects in ATP-sensitive Potassium Channels Caused by
780 Sulfonylurea Receptor 1 Mutations. J Biol Chem. 2016;291(42):21971-83. doi:
781 10.1074/jbc.M116.749366. PubMed PMID: 27573238; PubMed Central PMCID: PMCPMC5063981.

782 12. Tian M, Ye S. Allosteric regulation in NMDA receptors revealed by the genetically encoded
783 photo-cross-linkers. Sci Rep. 2016;6:34751. doi: 10.1038/srep34751. PubMed PMID: 27713495;
784 PubMed Central PMCID: PMCPMC5054432.
785 13. Rannversson H, Andersen J, Sorensen L, Bang-Andersen B, Park M, Huber T, et al.
786 Genetically encoded photocrosslinkers locate the high-affinity binding site of antidepressant drugs
787 in the human serotonin transporter. Nat Commun. 2016;7:11261. doi: 10.1038/ncomms11261.
788 PubMed PMID: 27089947; PubMed Central PMCID: PMCPMC4838859.
789 14. Coin I, Katritch V, Sun T, Xiang Z, Siu FY, Beyermann M, et al. Genetically encoded chemical
790 probes in cells reveal the binding path of urocortin-I to CRF class B GPCR. Cell. 2013;155(6):1258-
791 69. doi: 10.1016/j.cell.2013.11.008. PubMed PMID: 24290358; PubMed Central PMCID:
792 PMC3916339.
793 15. Bottke T, Ernicke S, Serfling R, Ihling C, Burda E, Gurevich VV, et al. Exploring GPCR-
794 arrestin interfaces with genetically encoded crosslinkers. EMBO Rep. 2020:e50437. doi:
795 10.15252/embr.202050437. PubMed PMID: 32929862.
796 16. Reiners M, Margreiter MA, Oslender-Bujotzek A, Rossetti G, Grunder S, Schmidt A. The
797 Conorfamide RPRFa Stabilizes the Open Conformation of Acid-Sensing Ion Channel 3 via the
798 Nonproton Ligand-Sensing Domain. Mol Pharmacol. 2018;94(4):1114-24. doi:
799 10.1124/mol.118.112375. PubMed PMID: 30012583.
800 17. Borg CB, Braun N, Heusser SA, Bay Y, Weis D, Galleano I, et al. Mechanism and site of
801 action of big dynorphin on ASIC1a. Proc Natl Acad Sci U S A. 2020;117(13):7447-54. doi:
802 10.1073/pnas.1919323117. PubMed PMID: 32165542; PubMed Central PMCID:
803 PMCPMC7132280.
804 18. Kuenze G, Vanoye CG, Desai RR, Adusumilli S, Brewer KR, Woods H, et al. Allosteric
805 mechanism for KCNE1 modulation of KCNQ1 potassium channel activation. Elife. 2020;9. doi:
806 10.7554/eLife.57680. PubMed PMID: 33095155; PubMed Central PMCID: PMCPMC7584456.
807 19. Shen W, Ren W, Zhai S, Yang B, Vanoye CG, Mitra A, et al. Striatal Kir2 K+ channel inhibition
808 mediates the antidyskinetic effects of amantadine. J Clin Invest. 2020;130(5):2593-601. doi:
809 10.1172/JCI133398. PubMed PMID: 32310223; PubMed Central PMCID: PMCPMC7190977.
810 20. Silvera Ejneby M, Wallner B, Elinder F. Coupling stabilizers open KV1-type potassium
811 channels. Proc Natl Acad Sci U S A. 2020;117(43):27016-21. doi: 10.1073/pnas.2007965117.
812 PubMed PMID: 33051293; PubMed Central PMCID: PMCPMC7604479.
813 21. Xu H, Li T, Rohou A, Arthur CP, Tzakoniati F, Wong E, et al. Structural Basis of Nav1.7
814 Inhibition by a Gating-Modifier Spider Toxin. Cell. 2019;176(4):702-15 e14. doi:
815 10.1016/j.cell.2018.12.018. PubMed PMID: 30661758.
816 22. Chernov-Rogan T, Li T, Lu G, Verschoof H, Khakh K, Jones SW, et al. Mechanism-specific
817 assay design facilitates the discovery of Nav1.7-selective inhibitors. Proc Natl Acad Sci U S A.
818 2018;115(4):E792-E801. doi: 10.1073/pnas.1713701115. PubMed PMID: 29311306; PubMed
819 Central PMCID: PMCPMC5789920.

820 23. Rook ML, Musgaard M, MacLean DM. Coupling structure with function in acid-sensing ion
821 channels: challenges in pursuit of proton sensors. J Physiol. 2020. doi: 10.1113/JP278707. PubMed
822 PMID: 32306405.
823 24. Wemmie JA, Taugher RJ, Kreple CJ. Acid-sensing ion channels in pain and disease. Nat
824 Rev Neurosci. 2013;14(7):461-71. doi: 10.1038/nrn3529. PubMed PMID: 23783197; PubMed
825 Central PMCID: PMC4307015.
826 25. Vullo S, Kellenberger S. A molecular view of the function and pharmacology of acid-sensing
827 ion channels. Pharmacol Res. 2020;154:104166. doi: 10.1016/j.phrs.2019.02.005. PubMed PMID:
828 30731197.
829 26. Diochot S, Baron A, Salinas M, Douguet D, Scarzello S, Dabert-Gay AS, et al. Black mamba
830 venom peptides target acid-sensing ion channels to abolish pain. Nature. 2012;490(7421):552-5.
831 doi: 10.1038/nature11494. PubMed PMID: 23034652.
832 27. Verkest C, Piquet E, Diochot S, Dauvois M, Lanteri-Minet M, Lingueglia E, et al. Effects of
833 systemic inhibitors of acid-sensing ion channels 1 (ASIC1) against acute and chronic mechanical
834 allodynia in a rodent model of migraine. Br J Pharmacol. 2018;175(21):4154-66. doi:
835 10.1111/bph.14462. PubMed PMID: 30079481; PubMed Central PMCID: PMCPMC6177611.
836 28. Bohlen CJ, Chesler AT, Sharif-Naeini R, Medzihradszky KF, Zhou S, King D, et al. A
837 heteromeric Texas coral snake toxin targets acid-sensing ion channels to produce pain. Nature.
838 2011;479(7373):410-4. doi: 10.1038/nature10607. PubMed PMID: 22094702; PubMed Central
839 PMCID: PMC3226747.
840 29. Lee JYP, Saez NJ, Cristofori-Armstrong B, Anangi R, King GF, Smith MT, et al. Inhibition of
841 acid-sensing ion channels by diminazene and APETx2 evoke partial and highly variable
842 antihyperalgesia in a rat model of inflammatory pain. Br J Pharmacol. 2018;175(12):2204-18. Epub
843 2017/11/15. doi: 10.1111/bph.14089. PubMed PMID: 29134638; PubMed Central PMCID:
844 PMCPMC5980509.
845 30. Reimers C, Lee CH, Kalbacher H, Tian Y, Hung CH, Schmidt A, et al. Identification of a cono-
846 RFamide from the venom of Conus textile that targets ASIC3 and enhances muscle pain. Proc Natl
847 Acad Sci U S A. 2017;114(17):E3507-E15. Epub 2017/04/12. doi: 10.1073/pnas.1616232114.
848 PubMed PMID: 28396446; PubMed Central PMCID: PMCPMC5410773.
849 31. Xiong ZG, Zhu XM, Chu XP, Minami M, Hey J, Wei WL, et al. Neuroprotection in ischemia:
850 blocking calcium-permeable acid-sensing ion channels. Cell. 2004;118(6):687-98. Epub 2004/09/17.
851 doi: 10.1016/j.cell.2004.08.026. PubMed PMID: 15369669.
852 32. Wang YZ, Wang JJ, Huang Y, Liu F, Zeng WZ, Li Y, et al. Tissue acidosis induces neuronal
853 necroptosis via ASIC1a channel independent of its ionic conduction. Elife. 2015;4. doi:
854 10.7554/eLife.05682. PubMed PMID: 26523449; PubMed Central PMCID: PMCPMC4629285.
855 33. Wang JJ, Liu F, Yang F, Wang YZ, Qi X, Li Y, et al. Disruption of auto-inhibition underlies
856 conformational signaling of ASIC1a to induce neuronal necroptosis. Nat Commun. 2020;11(1):475.

857 doi: 10.1038/s41467-019-13873-0. PubMed PMID: 31980622; PubMed Central PMCID:
858 PMCPMC6981194.
859 34. Chassagnon IR, McCarthy CA, Chin YK, Pineda SS, Keramidas A, Mobli M, et al. Potent
860 neuroprotection after stroke afforded by a double-knot spider-venom peptide that inhibits acid-
861 sensing ion channel 1a. Proc Natl Acad Sci U S A. 2017;114(14):3750-5. Epub 2017/03/23. doi:
862 10.1073/pnas.1614728114. PubMed PMID: 28320941; PubMed Central PMCID:
863 PMCPMC5389327.
864 35. McCarthy CA, Rash LD, Chassagnon IR, King GF, Widdop RE. PcTx1 affords
865 neuroprotection in a conscious model of stroke in hypertensive rats via selective inhibition of ASIC1a.
866 Neuropharmacology. 2015;99:650-7. Epub 2015/09/01. doi: 10.1016/j.neuropharm.2015.08.040.
867 PubMed PMID: 26320544.
868 36. Rash LD. Acid-Sensing Ion Channel Pharmacology, Past, Present, and Future. Adv
869 Pharmacol. 2017;79:35-66. Epub 2017/05/23. doi: 10.1016/bs.apha.2017.02.001. PubMed PMID:
870 28528673.
871 37. Vyvers A, Schmidt A, Wiemuth D, Grunder S. Screening of 109 neuropeptides on ASICs
872 reveals no direct agonists and dynorphin A, YFMRFamide and endomorphin-1 as modulators. Sci
873 Rep. 2018;8(1):18000. doi: 10.1038/s41598-018-36125-5. PubMed PMID: 30573735; PubMed
874 Central PMCID: PMCPMC6301962.
875 38. Baron A, Diochot S, Salinas M, Deval E, Noel J, Lingueglia E. Venom toxins in the exploration
876 of molecular, physiological and pathophysiological functions of acid-sensing ion channels. Toxicon.
877 2013;75:187-204. Epub 2013/04/30. doi: 10.1016/j.toxicon.2013.04.008. PubMed PMID: 23624383.
878 39. Cristofori-Armstrong B, Saez NJ, Chassagnon IR, King GF, Rash LD. The modulation of acid-
879 sensing ion channel 1 by PcTx1 is pH-, subtype- and species-dependent: Importance of interactions
880 at the channel subunit interface and potential for engineering selective analogues. Biochem
881 Pharmacol. 2019;163:381-90. doi: 10.1016/j.bcp.2019.03.004. PubMed PMID: 30849303.
882 40. Sherwood TW, Askwith CC. Dynorphin opioid peptides enhance acid-sensing ion channel 1a
883 activity and acidosis-induced neuronal death. J Neurosci. 2009;29(45):14371-80. doi:
884 10.1523/JNEUROSCI.2186-09.2009. PubMed PMID: 19906984; PubMed Central PMCID:
885 PMC2802056.
886 41. Escoubas P, De Weille JR, Lecoq A, Diochot S, Waldmann R, Champigny G, et al. Isolation
887 of a tarantula toxin specific for a class of proton-gated Na+ channels. J Biol Chem.
888 2000;275(33):25116-21. doi: 10.1074/jbc.M003643200. PubMed PMID: 10829030.
889 42. Ye S, Kohrer C, Huber T, Kazmi M, Sachdev P, Yan EC, et al. Site-specific incorporation of
890 keto amino acids into functional G protein-coupled receptors using unnatural amino acid
891 mutagenesis. J Biol Chem. 2008;283(3):1525-33. doi: 10.1074/jbc.M707355200. PubMed PMID:
892 17993461.

893 43. Ye S, Huber T, Vogel R, Sakmar TP. FTIR analysis of GPCR activation using azido probes.
894 Nat Chem Biol. 2009;5(6):397-9. doi: 10.1038/nchembio.167. PubMed PMID: 19396177; PubMed
895 Central PMCID: PMCPMC2875874.
896 44. Chatterjee A, Xiao H, Bollong M, Ai HW, Schultz PG. Efficient viral delivery system for
897 unnatural amino acid mutagenesis in mammalian cells. P Natl Acad Sci USA. 2013;110(29):11803-
898 8. doi: 10.1073/pnas.1309584110. PubMed PMID: WOS:000322086100042.
899 45. Gordon SE, Munari M, Zagotta WN. Visualizing conformational dynamics of proteins in
900 solution and at the cell membrane. Elife. 2018;7. doi: 10.7554/eLife.37248. PubMed PMID:
901 29923827; PubMed Central PMCID: PMCPMC6056233.
902 46. Sherwood TW, Askwith CC. Endogenous arginine-phenylalanine-amide-related peptides
903 alter steady-state desensitization of ASIC1a. J Biol Chem. 2008;283(4):1818-30. Epub 2007/11/07.
904 doi: 10.1074/jbc.M705118200. PubMed PMID: 17984098.
905 47. Vaithia A, Vullo S, Peng Z, Alijevic O, Kellenberger S. Accelerated Current Decay Kinetics of
906 a Rare Human Acid-Sensing ion Channel 1a Variant That Is Used in Many Studies as Wild Type.
907 Front Mol Neurosci. 2019;12:133. doi: 10.3389/fnmol.2019.00133. PubMed PMID: 31178694;
908 PubMed Central PMCID: PMCPMC6542941.
909 48. Kasimova MA, Lynagh T, Sheikh ZP, Granata D, Borg CB, Carnevale V, et al. Evolutionarily
910 Conserved Interactions within the Pore Domain of Acid-Sensing Ion Channels. Biophys J.
911 2020;118(4):861-72. doi: 10.1016/j.bpj.2019.09.001. PubMed PMID: 31630811; PubMed Central
912 PMCID: PMCPMC7036722.
913 49. Chen X, Grunder S. Permeating protons contribute to tachyphylaxis of the acid-sensing ion
914 channel (ASIC) 1a. J Physiol. 2007;579(Pt 3):657-70. Epub 2007/01/06. doi:
915 10.1113/jphysiol.2006.120733. PubMed PMID: 17204502; PubMed Central PMCID:
916 PMCPMC2151377.
917 50. Gasparri F, Wengel J, Grutter T, Pless SA. Molecular determinants for agonist recognition
918 and discrimination in P2X2 receptors. J Gen Physiol. 2019;151(7):898-911. doi:
919 10.1085/jgp.201912347. PubMed PMID: 31126967; PubMed Central PMCID: PMCPMC6605687.
920 51. Yamada KA, Tang CM. Benzothiadiazides inhibit rapid glutamate receptor desensitization
921 and enhance glutamatergic synaptic currents. J Neurosci. 1993;13(9):3904-15. PubMed PMID:
922 8103555; PubMed Central PMCID: PMCPMC6576449.
923 52. Baconguis I, Gouaux E. Structural plasticity and dynamic selectivity of acid-sensing ion
924 channel-spider toxin complexes. Nature. 2012;489(7416):400-5. Epub 2012/07/31. doi:
925 10.1038/nature11375. PubMed PMID: 22842900; PubMed Central PMCID: PMCPMC3725952.
926 53. Liu Y, Hagan R, Schoellerman J. Dual actions of Psalmotoxin at ASIC1a and ASIC2a
927 heteromeric channels (ASIC1a/2a). Sci Rep. 2018;8(1):7179. doi: 10.1038/s41598-018-25386-9.
928 PubMed PMID: 29739981; PubMed Central PMCID: PMCPMC5940917.
929 54. Salinas M, Rash LD, Baron A, Lambeau G, Escoubas P, Lazdunski M. The receptor site of
930 the spider toxin PcTx1 on the proton-gated cation channel ASIC1a. J Physiol. 2006;570(Pt 2):339-

931 54. doi: 10.1113/jphysiol.2005.095810. PubMed PMID: 16284080; PubMed Central PMCID:
932 PMC1464308.
933 55. Ahmed R, Spikings E, Zhou S, Thompsett A, Zhang T. Pre-hybridisation: an efficient way of
934 suppressing endogenous biotin-binding activity inherent to biotin-streptavidin detection system. J
935 Immunol Methods. 2014;406:143-7. doi: 10.1016/j.jim.2014.03.010. PubMed PMID: 24657589.
936 56. Praul CA, Brubaker KD, Leach RM, Gay CV. Detection of endogenous biotin-containing
937 proteins in bone and cartilage cells with streptavidin systems. Biochem Biophys Res Commun.
938 1998;247(2):312-4. doi: 10.1006/bbrc.1998.8757. PubMed PMID: 9642122.
939 57. Sherwood T, Franke R, Conneely S, Joyner J, Arumugan P, Askwith C. Identification of
940 protein domains that control proton and calcium sensitivity of ASIC1a. J Biol Chem.
941 2009;284(41):27899-907. doi: 10.1074/jbc.M109.029009. PubMed PMID: 19654327; PubMed
942 Central PMCID: PMC2788841.
943 58. Saez NJ, Deplazes E, Cristofori-Armstrong B, Chassagnon IR, Lin X, Mobli M, et al.
944 Molecular dynamics and functional studies define a hot spot of crystal contacts essential for PcTx1
945 inhibition of acid-sensing ion channel 1a. Br J Pharmacol. 2015;172(20):4985-95. doi:
946 10.1111/bph.13267. PubMed PMID: 26248594; PubMed Central PMCID: PMC4621980.
947 59. Obergrussberger A, Friis S, Bruggemann A, Fertig N. Automated patch clamp in drug
948 discovery: major breakthroughs and innovation in the last decade. Expert Opin Drug Discov. 2020:1-
949 5. doi: 10.1080/17460441.2020.1791079. PubMed PMID: 32646308.
950 60. Ke YY, Huang YH, Chien WC, Loh HH, Chuang JY, Yeh SH. Mapping the naloxone binding
951 sites on the mu-opioid receptor using cell-based photocrosslinkers. Biochim Biophys Acta Proteins
952 Proteom. 2017;1865(3):336-43. doi: 10.1016/j.bbapap.2016.12.010. PubMed PMID: 28012872.
953 61. Hostetler ZM, Ferrie JJ, Bornstein MR, Sungwienwong I, Petersson EJ, Kohli RM. Systematic
954 Evaluation of Soluble Protein Expression Using a Fluorescent Unnatural Amino Acid Reveals No
955 Reliable Predictors of Tolerability. Acs Chemical Biology. 2018;13(10):2855-61. doi:
956 10.1021/acschembio.8b00696. PubMed PMID: WOS:000448488600005.
957 62. Coscoy S, de Weille JR, Lingueglia E, Lazdunski M. The pre-transmembrane 1 domain of
958 acid-sensing ion channels participates in the ion pore. J Biol Chem. 1999;274(15):10129-32.
959 PubMed PMID: 10187795.
960 63. Lynagh T, Flood E, Boiteux C, Wulf M, Komnatnyy VV, Colding JM, et al. A selectivity filter
961 at the intracellular end of the acid-sensing ion channel pore. Elife. 2017;6. Epub 2017/05/13. doi:
962 10.7554/eLife.24630. PubMed PMID: 28498103; PubMed Central PMCID: PMCPMC5449180.
963 64. Krauson AJ, Carattino MD. The Thumb Domain Mediates Acid-sensing Ion Channel
964 Desensitization. J Biol Chem. 2016;291(21):11407-19. doi: 10.1074/jbc.M115.702316. PubMed
965 PMID: 27015804; PubMed Central PMCID: PMCPMC4900284.
966 65. MacLean DM, Jayaraman V. Deactivation kinetics of acid-sensing ion channel 1a are strongly
967 pH-sensitive. Proc Natl Acad Sci U S A. 2017;114(12):E2504-E13. Epub 2017/03/08. doi:

968 10.1073/pnas.1620508114. PubMed PMID: 28265090; PubMed Central PMCID:
969 PMCPMC5373395.
970 66. Li T, Yang Y, Canessa CM. Impact of recovery from desensitization on acid-sensing ion
971 channel-1a (ASIC1a) current and response to high frequency stimulation. J Biol Chem.
972 2012;287(48):40680-9. Epub 2012/10/11. doi: 10.1074/jbc.M112.418400. PubMed PMID:
973 23048040; PubMed Central PMCID: PMCPMC3504781.
974 67. Dawson RJ, Benz J, Stohler P, Tetaz T, Joseph C, Huber S, et al. Structure of the acid-
975 sensing ion channel 1 in complex with the gating modifier Psalmotoxin 1. Nat Commun. 2012;3:936.
976 doi: 10.1038/ncomms1917. PubMed PMID: 22760635.
977 68. O'Connor C, White KL, Doncescu N, Didenko T, Roth BL, Czaplicki G, et al. NMR structure
978 and dynamics of the agonist dynorphin peptide bound to the human kappa opioid receptor. Proc Natl
979 Acad Sci U S A. 2015;112(38):11852-7. doi: 10.1073/pnas.1510117112. PubMed PMID: 26372966;
980 PubMed Central PMCID: PMCPMC4586840.
981 69. Ferre G, Czaplicki G, Demange P, Milon A. Structure and dynamics of dynorphin peptide and
982 its receptor. Vitam Horm. 2019;111:17-47. doi: 10.1016/bs.vh.2019.05.006. PubMed PMID:
983 31421700.
984 70. Grunbeck A, Huber T, Sachdev P, Sakmar TP. Mapping the ligand-binding site on a G
985 protein-coupled receptor (GPCR) using genetically encoded photocrosslinkers. Biochemistry.
986 2011;50(17):3411-3. doi: 10.1021/bi200214r. PubMed PMID: 21417335; PubMed Central PMCID:
987 PMCPMC3099303.
988 71. Dorman G, Prestwich GD. Benzophenone photophores in biochemistry. Biochemistry.
989 1994;33(19):5661-73. PubMed PMID: 8180191.
990 72. Ai HW, Shen W, Sagi A, Chen PR, Schultz PG. Probing protein-protein interactions with a
991 genetically encoded photo-crosslinking amino acid. Chembiochem. 2011;12(12):1854-7. doi:
992 10.1002/cbic.201100194. PubMed PMID: 21678540.
993 73. Calloe K, Rognant S, Friis S, Shaughnessy C, Klaerke DA, Trachsel D. Compounds
994 commonly used in equine medicine inhibits the voltage-gated potassium channel Kv11.1. Res Vet
995 Sci. 2019;123:239-46. doi: 10.1016/j.rvsc.2019.01.009. PubMed PMID: 30685649.
996 74. Sauter DR, Sorensen CE, Rapedius M, Bruggemann A, Novak I. pH-sensitive K(+) channel
997 TREK-1 is a novel target in pancreatic cancer. Biochim Biophys Acta. 2016;1862(10):1994-2003.
998 doi: 10.1016/j.bbadis.2016.07.009. PubMed PMID: 27443495.
999 75. Ghovanloo MR, Shuart NG, Mezeyova J, Dean RA, Ruben PC, Goodchild SJ. Inhibitory
1000 effects of cannabidiol on voltage-dependent sodium currents. J Biol Chem. 2018;293(43):16546-58.
1001 doi: 10.1074/jbc.RA118.004929. PubMed PMID: 30219789; PubMed Central PMCID:
1002 PMCPMC6204917.
1003 76. Franz D, Olsen HL, Klink O, Gimsa J. Automated and manual patch clamp data of human
1004 induced pluripotent stem cell-derived dopaminergic neurons. Sci Data. 2017;4:170056. doi:
1005 10.1038/sdata.2017.56. PubMed PMID: 28440808; PubMed Central PMCID: PMCPMC5404656.

1006 77. Gupta K, Toombes GE, Swartz KJ. Exploring structural dynamics of a membrane protein by
1007 combining bioorthogonal chemistry and cysteine mutagenesis. Elife. 2019;8. doi:
1008 10.7554/eLife.50776. PubMed PMID: 31714877; PubMed Central PMCID: PMCPMC6850778.
1009 78. Piotrowski C, Ihling CH, Sinz A. Extending the cross-linking/mass spectrometry strategy:
1010 Facile incorporation of photo-activatable amino acids into the model protein calmodulin in
1011 Escherichia coli cells. Methods. 2015;89:121-7. doi: 10.1016/j.ymeth.2015.02.012. PubMed PMID:
1012 25726908.
1013 79. Boddum K, Skafte-Pedersen P, Rolland JF, Wilson S. Optogenetics and Optical Tools in
1014 Automated Patch Clamping. Methods Mol Biol. 2021;2188:311-30. doi: 10.1007/978-1-0716-0818-
1015 0_16. PubMed PMID: 33119859.
1016 80. Hoffmann JE. Bifunctional Non-Canonical Amino Acids: Combining Photo-Crosslinking with
1017 Click Chemistry. Biomolecules. 2020;10(4). doi: 10.3390/biom10040578. PubMed PMID: 32290035;
1018 PubMed Central PMCID: PMCPMC7226127.
1019 81. Wu X, Spence JS, Das T, Yuan X, Chen C, Zhang Y, et al. Site-Specific Photo-Crosslinking
1020 Proteomics Reveal Regulation of IFITM3 Trafficking and Turnover by VCP/p97 ATPase. Cell Chem
1021 Biol. 2020;27(5):571-85 e6. doi: 10.1016/j.chembiol.2020.03.004. PubMed PMID: 32243810;
1022 PubMed Central PMCID: PMCPMC7194980.
1023 82. Dumas A, Lercher L, Spicer CD, Davis BG. Designing logical codon reassignment -
1024 Expanding the chemistry in biology. Chem Sci. 2015;6(1):50-69. doi: 10.1039/c4sc01534g. PubMed
1025 PMID: 28553457; PubMed Central PMCID: PMCPMC5424465.
1026 83. Schmied WH, Elsasser SJ, Uttamapinant C, Chin JW. Efficient multisite unnatural amino acid
1027 incorporation in mammalian cells via optimized pyrrolysyl tRNA synthetase/tRNA expression and
1028 engineered eRF1. J Am Chem Soc. 2014;136(44):15577-83. doi: 10.1021/ja5069728. PubMed
1029 PMID: 25350841; PubMed Central PMCID: PMCPMC4333590.
1030 84. Kalstrup T, Blunck R. Reinitiation at non-canonical start codons leads to leak expression
1031 when incorporating unnatural amino acids. Scientific reports. 2015;5:11866. Epub 2015/07/15. doi:
1032 10.1038/srep11866. PubMed PMID: 26153354; PubMed Central PMCID: PMCPMC4648390.

1033